Journal of Thermal Analysis and Calorimetry (2024) 149:5341–5365
https://doi.org/10.1007/s10973-024-13159-8

A synergistic approach to optimizing the performance of a concentrating solar segmented variable area leg thermoelectric generator using numerical methods and neural networks

Hisham Alghamdi[1] · Chika Maduabuchi[2] · Abdullah Albaker[3] · Ibrahim Alatawi[4] · Theyab R. Alsenani[5] · Ahmed S. Alsafran[6] · Mohammed AlAqil[6] · Mohammad Alkhedher[7]

Received: 22 April 2023 / Accepted: 31 March 2024 / Published online: 8 May 2024

Abstract
This study presents an optimized design for segmented variable area leg thermoelectric modules using finite element methods and Bayesian regularized neural networks. We explored the impact of geometry and thermal parameters on module performance using ANSYS software, identifying optimal parameters for power output and efficiency. Key findings revealed the higher influence of geometric parameters and confirmed the advantages of segmented thermoelectric generators for high-temperature applications like concentrated solar systems. With this optimization, power output and efficiency of the module increased by 875% and 165%, respectively, under 25 Suns. To refine the optimization process, a Bayesian regularized neural network was utilized, proving effective in predicting module performance with a low mean squared error and high coefficient of determination. This research provides important insights into high-performance thermoelectric modules for sustainable energy applications, demonstrating the significant role of advanced computational methods in energy solutions.

Keywords Bayesian regularization · Finite element · Neural networks · Solar energy · Thermoelectric generator

✉ Chika Maduabuchi
chika.maduabuchi.191341@unn.edu.ng

✉ Theyab R. Alsenani
t.alsenani@psau.edu.sa

[1] Electrical Engineering Department, College of Engineering, Najran University, 55461 Najran, Saudi Arabia

[2] Artificial Intelligence Laboratory, University of Nigeria Nsukka, Nsukka, Enugu 410001, Nigeria

[3] Department of Electrical Engineering, College of Engineering, University of Ha'il, 81451 Ha'il, Saudi Arabia

[4] Department of Mechanical Engineering, College of Engineering, University of Ha'il, 81451 Ha'il, Saudi Arabia

[5] Department of Electrical Engineering, College of Engineering in Al-Kharj, Prince Sattam Bin Abdulaziz University, 11942 Al-Kharj, Saudi Arabia

[6] Department of Electrical Engineering, College of Engineering, King Faisal University, 31982 Al Ahsa, Saudi Arabia

[7] Department of Mechanical and Industrial Engineering, Abu Dhabi University, 59911 Abu Dhabi, United Arab Emirates

List of symbols

ΔT	Temperature gradient, K
3D	Three-dimensional
A	Area, m^2
C	Concentration ratio
CG	Concentrated heat flux, kWm^{-2}
G	Global solar irradiance, Wm^{-2}
H	Heat transfer coefficient, Wm^{-2} K^{-1}
J	Current density, Am^{-2}
k	Thermal conductivity, Wm^{-1} K^{-1}
L	Height, mm
P	Power output, W
Q	Heat flow rate, W
R	Electrical resistance, Ω
S	Seebeck coefficient, VK^{-1}
T	Temperature, K
w	Wind speed, ms^{-1}

Subscripts

conv	Convective
g	Glass
h	Hot junction
in	Input
n	N-leg
rad	Radiation

s Selective surface
sky Sky

Greek symbols

α Absorptivity
β Thomson coefficient, K^{-1}, regularization parameter
ε Emissivity
η Efficiency, %
ϖ Electric field scalar potential, V
ρ Electrical resistivity, Ω m
σ Stefan–Boltzmann constant, Wm^{-2} K^{-4}
τ Transmissivity

Introduction

Thermoelectric generators (TEGs) play a significant role in various applications today, from effective solar power generation [1] to waste heat recovery on human skin [2] and automobile exhaust systems [3]. These devices can directly transform thermal energy into electricity without relying on moving parts, making them a promising option for sustainable energy generation [4]. However, their limited power output and overall performance [5] hinder their widespread adoption. Despite numerous efforts to address these shortcomings [6], further enhancements are needed before TEGs can be considered a viable alternative for renewable energy generation.

Numerous researchers have employed material property modification as a strategy to enhance the performance of thermoelectric devices [7, 8]. Zhang et al. [9] proposed a hybrid system consisting of a heat pipe reactor and a segmented thermoelectric generator, using a three-dimensional finite element method in COMSOL software. The generator featured stacked bismuth-telluride and skutterudite materials in its *n*- and *p*-type legs. Through optimization of geometry parameters and operating conditions, the device achieved a maximum output power of 0.374 W and an efficiency of 15.75% with a 550 K temperature gradient. Sharma and Debbarma [10] improved the performance of a segmented thermoelectric generator by adjusting the geometry dimensions of the middle materials in the *p*-legs. Using the ANSYS finite element solver, they examined the effects of hot junction temperature, load resistance, and copper conductor thickness. Their results showed a maximum power of 47 W at an optimal load resistance ratio of unity. Cao et al. [11] achieved a 13.6% efficiency with a modest 493 K temperature difference by conducting compatibility factor analysis to design an efficient segmented thermoelectric generator, using finite elements and experimental analysis. They discovered that modifying the heights of skutterudite and bismuth-telluride segments influenced thermoelectric efficiency. Zhao et al. [12] introduced a seven-layer, segmented thermoelectric generator with four thermoelectric materials in each pin. They applied an ensemble-based regressive neural network to explore the relationship between material properties and device power and efficiency. By selecting the optimal thermoelectric material for each segment, the generator achieved a power of 184.1 mW and an efficiency of 16.7%, which were 86.14% and 31.19% higher than a traditional thermoelectric generator, respectively. Demeke et al. [13] suggested a rapid, deep learning technique combined with a genetic algorithm and finite element method to investigate and optimize the design of efficient segmented thermoelectric generators. They noted that their proposed neural network prediction approach reduced computational time compared to traditional finite element methods that rely on extensive computation.

Variable area leg thermoelectric modules have garnered considerable interest within the scientific community due to their potential to enhance the power conversion efficiency of traditional uniform leg devices under similar operating conditions [14]. Weng et al. [15] improved the performance of traditional annular thermoelectric generators by using variable angle thermoelectric legs and finite element modeling, subject to various boundary conditions. Their results show that the shape of the variable angle leg significantly influences the performance of the thermoelectric generator, with a 35% performance increase when the leg radius was set to 2. Ge et al. [16] aimed to boost the output power of variable leg thermoelectric generators by integrating finite element method, genetic algorithm, and particle swarm optimization. They suggested that modifying the leg shape increased the thermoelectric figure of merit, subsequently enhancing the device output power and efficiency. With optimized device usage, the temperature difference and output power of the variable leg thermoelectric generator improved by 73% and 20%, respectively, at a heat flux of 50 kWm^{-2}. Wang et al. [17] proposed a frustum-shaped thermoelectric leg to address the low performance issue of thermoelectric generators. After optimizing the geometry, the variable leg thermoelectric generator increased the device output power by 96.64% without compromising conversion efficiency. Siddique et al. [18] compared the performance of trapezoidal leg and traditional rectangular leg thermoelectric generators produced through the dispenser printing method. They found that the output power of the variable leg thermoelectric generator was 1.5 times higher than that of the conventional design. Wang et al. [19] suggested that variable area thermoelectric pins could be the key to designing highly efficient thermoelectric generators, as material performance improvements are nearing their limits. They emphasized that reducing leg electrical resistance and material volume are crucial for achieving higher power and efficiency. Additionally, they observed that geometry optimization led to a 43% and 9.67% increase in device power and efficiency, respectively.

The previous subsections demonstrate that using segmented materials and variable legs can enhance device performance. By combining these approaches to create a segmented variable leg thermoelectric generator, it may be possible to achieve even higher power output and efficiency. However, only a few studies have explored this complex system design, and they have made unrealistic assumptions, such as analyzing a single thermoelectric couple while neglecting the impact of mutual interactions between numerous thermocouples on the design results. Liu et al. [20] developed a segmented variable leg thermoelectric couple to improve the performance of conventional thermoelectric couples, using the COMSOL finite element solver. They found that segmenting uniform leg pins increased device power by 15% after geometry optimization, while segmenting variable leg pins boosted power output by 4.21%. Shittu et al. [21] compared the performance of a segmented variable leg thermoelectric couple under transient and steady-state conditions using the COMSOL finite element solver. Their results showed that the proposed device improved the power output of traditional rectangular leg thermoelectric couple by 117% under rectangular pulsed heating. Lastly, Luo et al. [22] created a three-dimensional finite element model in ANSYS software to optimize the performance of a segmented thermoelectric generator with trapezoidal-shaped pins. They concluded that a combination of trapezoidal segmented p-legs and unsegmented rectangular n-legs yielded the highest efficiency when using high-temperature materials such as silicon germanium and skutterudite.

Neural networks are computing systems inspired by the thought processes of biological neurons that make up the human brain [23]. They consist of layers of interconnected elements, known as neurons, which transform input data to generate their own understanding [24]. The goal of neural networks is to enable computers to function more like the human brain [24]. Neurons offer several desirable advantages, such as the capability to accurately predict the performance of devices after being trained, even without extensive knowledge [25]. This ability has led to their increased use in predicting the experimental and theoretical performance of various renewable energy technologies, including solar radiation prediction [26], clean energy communities [27], photovoltaics [28], and thermoelectric generators [29]. Neural networks are highly efficient in predicting the performance of thermoelectric generators [30]. This is largely due to the substantial computational resources required by finite element solvers to predict thermoelectric module's performance [31]. The equations governing thermoelectric phenomena are quite complex, particularly when considering three-dimensional models with numerous thermocouples characterized by temperature-dependent materials [32]. However, neural networks can quickly predict thermoelectric generator performance without explicitly solving these complex, time-consuming equations [33, 34]. These networks are trained using data generated by numerical or experimental models, enabling them to readily predict device performance given arbitrary parameters. Once the neural network is trained, additional data generation becomes unnecessary. The neural network saves time and computational resources as it can predict thermoelectric generator performance beyond the generated dataset [29]. Kim et al. [35] employed a simple back-propagation neural network to predict the performance of a thermoelectric generator integrated into a diesel engine. The authors discovered that the neural network accurately predicted the experimental results without any errors. Wang et al. [36] improved the performance of a conventional thermoelectric generator by 182% after device optimization, facilitated by a simple back-propagation neural network.

In contrast with standard back-propagation algorithms used in neural networks, Bayesian regularized neural networks do not require lengthy cross-validation processes. These networks are more robust and can address the issue of overfitting/underfitting encountered in standard back-propagation algorithms [37]. One of the key advantages of Bayesian networks over standard back-propagation networks is their robustness, eliminating the need for lengthy validation processes [38]. Bayesian networks can be viewed as computational processes that transform a nonlinear regression problem into a well-defined statistical problem, such as ridge regression. The Bayesian regularized neural network achieves this by assigning a probability distribution to every mass and bias in the neural network. Additionally, unlike standard back-propagation algorithms, Bayesian regularized networks can solve problems even with limited data [39]. This advantage is particularly useful when generating the required data is challenging. Moreover, these networks naturally address issues like overfitting or underfitting of the model without needing a separate, lengthy cross-validation dataset, while maintaining acceptable generalization [40]. Bayesian regularized neural networks have been applied in predicting the operational state of centrifugal pumps [41], forecasting the operational voltages of deformable mirrors [42], and evaluating the characteristics of proton exchange membrane fuel cells [43]. However, despite these appealing advantages, Bayesian regularized neural networks have not yet been used to predict the performance of thermoelectric generators.

Based on the comprehensive literature review conducted, this research paper aims to address the following research gaps to make the segmented variable area leg thermoelectric generator a viable technology for solar power generation applications:

i. Ref. [17] focused on the numerical optimization of an unsegmented (single-material bismuth telluride) variable leg thermoelectric generator (frustum shape design) subjected to constant temperatures at the hot and cold junctions. In contrast, this study examines the segmented variable area leg design for concentrated solar energy conversion and power generation. This comparison highlights that the current work explores the thermal engineering analysis of a distinct device design (segmented pins) for a different application (solar energy harvesting). The variable area pins are segmented to enable practical applications under high heat flux conditions, a well-known concept in the thermoelectric community [44].

ii. Previous studies suggested that the optimal combination of segmented variable area leg TEGs could further enhance the TEG's performance [20–22]. However, due to the complexity of the numerical model involving 127 couples, only a single thermocouple was considered. This limitation restricted the computations performed and neglected the mutual interaction between the numerous semiconductors when determining the thermal distribution of the device under heat flux conditions. We address this gap by modeling the first full-scale, segmented variable leg TEG using our extensive computational facility, providing new insights into the optimum conditions for maximizing power and efficiency.

iii. Our approach advances beyond existing methods by employing Bayesian regularized neural networks for the first time to learn and predict the performance of the thermoelectric device. Prior works on using machine learning to facilitate thermoelectric design [30, 34, 36] relied on standard backpropagation neural networks for updating the network's masses. However, this method requires large amounts of training data and involves a lengthy cross-validation process that takes longer to reach the global optimum. In contrast, Bayesian regularization is more efficient than standard backpropagation, as it eliminates the need for lengthy cross-validation, requires only a small amount of data, and solves the problem of overfitting in neural networks. Moreover, it has never been applied to predict TEG performance. Our work is the first to utilize Bayesian regularized neural networks for predicting the performance of segmented variable area leg thermoelectric generators, offering a cost-effective, data-driven surrogate model that enables researchers to easily obtain optimal parameters from thermoelectric devices after an initial, one-time, computationally intensive data generation process using numerical methods.

Based on these, the key contributions of this research can be summarized as follows:

- Providing deeper insights into the optimal design of innovative segmented variable area leg thermoelectric generators by considering the mutual interaction of thermocouples in the full-scale module for efficient solar power generation applications.
- Enhancing and ultimately replacing traditional numerical methods used in the industry for designing these devices with the proposed augmented finite element method neural networks, which are faster, more efficient, and computationally less expensive. This facilitates the design and mass production of these devices.
- Substituting the standard backpropagation algorithms typically used for predicting the performance of thermoelectric devices with the more efficient Bayesian regularization algorithm. This method reduces overfitting using fewer datasets, further streamlining the design and production process of these devices for use in solar energy conversion applications.

The remaining sections of this work are organized as follows: a general description of the materials used to model the thermoelectric system is provided in "Materials and methods" section, while the equations governing the numerical method and Bayesian regularized neural network are provided in "Theoretical framework" section. The finite element method optimization, neural network tuning, numerical validation, and possible routes for fabricating the proposed device using 3D printing technology are discussed in "Results and discussion" section. Finally, the most important conclusions derived from the discussed results are presented in "Conclusions" section, along with suggestions for future research in this emerging field.

Materials and methods

In this section, we present the description of various materials and physical dimensions of each part of the segmented variable leg thermoelectric generator. Figure 1a illustrates the thermocouple considered in this study with surface dimensions of 40 mm × 40 mm. Global solar irradiance is received on the top glass of the solar concentrator and focused on the top ceramic plate of the thermoelectric generator as shown in Fig. 1b. The solar concentrator employed in this work is a compound parabolic concentrator with a solar concentration ratio of 50. The global solar irradiance is modeled assuming AM 1.5G weather conditions. The concentrated solar flux is converted to sensible thermal energy at the hot junction of the device by using a selective surface absorber placed on the top ceramic plate of the thermoelectric module, as shown in Fig. 1b. The surface area of the selective surface absorber is equal to

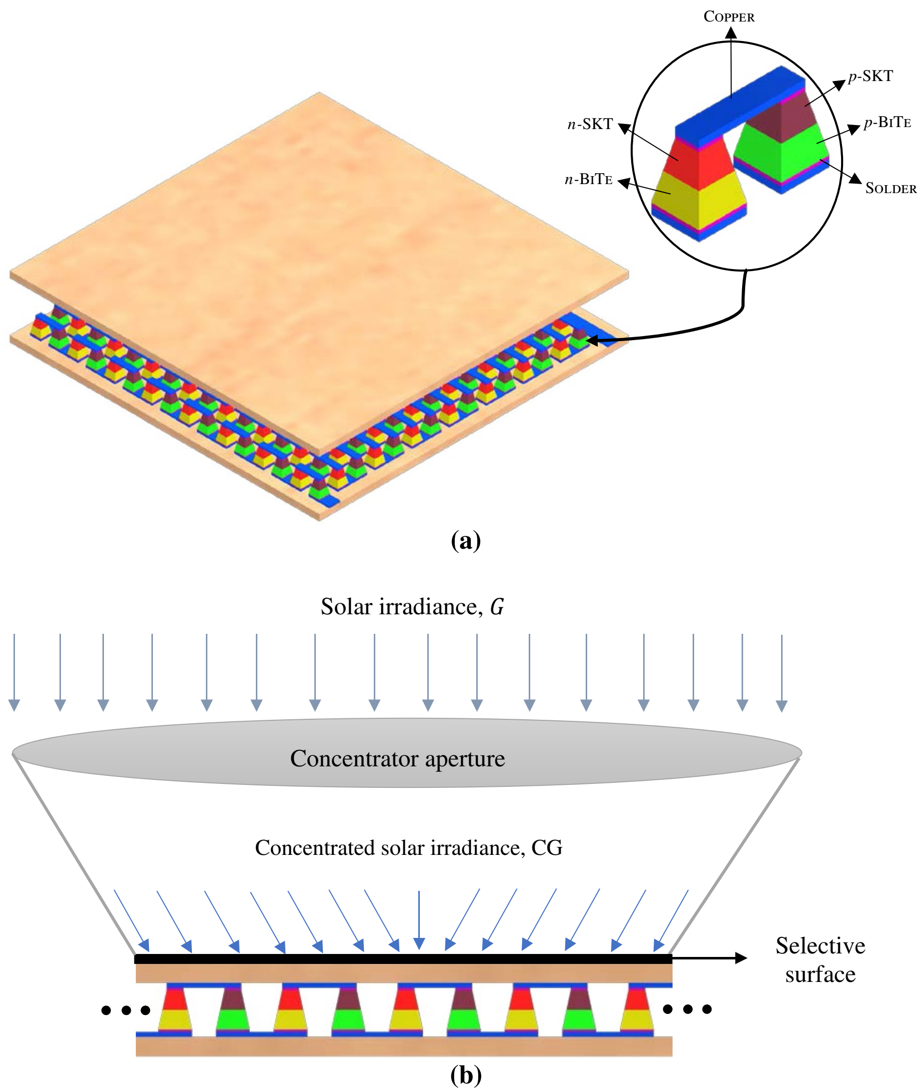

Fig. 1 Conceptual model of the modified full-scale thermoelectric module comprising 127 thermoelements reproduced using the design specifications of melcor thermoelectric [48]. **a** Exploded view of the thermoelectric couple shown in three-dimensions. *n*- and *p*- represent the *n*-type and *p*-type semiconductors while SKT and BiTe are the skutterudite and bismuth telluride semiconductors **b** illustration showing the top glass of the solar concentrator together with the selective surface absorber and top ceramic plate of the thermoelectric generator which formed the hot junction

that of the device's top ceramic plate, ensuring a uniform temperature distribution across the plate. The ceramic plates of the device are made of 96% alumina. Copper conductor pads are utilized to transfer the generated electrical energy from the thermoelectric legs to the connected external load. The device is assumed to operate under maximum power conditions; thus, the external load is considered equal to the thermoelectric internal resistance. The thermoelectric legs are connected to the copper conductor pads using lead-free solder interconnectors. The thermoelectric materials are composed of bismuth-telluride in the cold segment and skutterudite in the hot segment. Figure 2 depicts the temperature-dependent behaviors of these thermoelectric materials. The plot clearly demonstrates the optimal performance of skutterudite materials under high temperature differences reaching 1000 K. The properties of the other materials can be found in references [45–47].

Theoretical framework

In this section, we present the governing equations of thermoelectricity alongside the expressions used to determine the performance of the proposed device. Additionally, we describe the theoretical framework of the Bayesian regularized neural network and explain the data generation process using finite elements. Finally, the verification of the numerical model is conducted by comparisons with previous experimental and theoretical works.

Thermoelectric equations

The operation of the thermoelectric device is associated with the coupling of thermal and electrical governing equations in three dimensions, considering the temperature dependency of each material in the thermoelements. The governing equations also consider all thermoelectric effects responsible

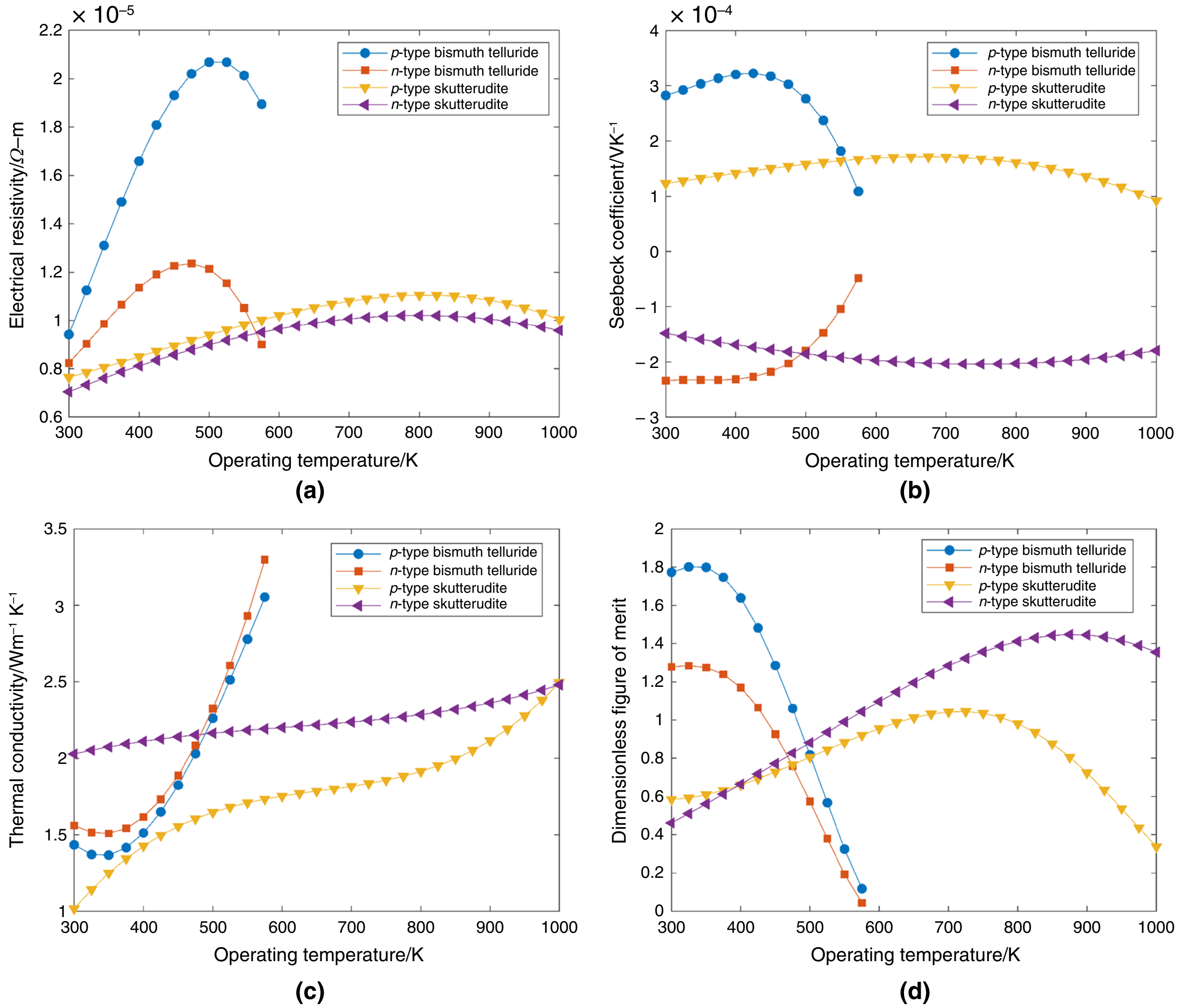

Fig. 2 Behavior of the thermoelectric material properties as the operating temperature in the segments change **a** electrical resistivity **b** Seebeck coefficient **c** thermal conductivity **d** dimensionless figure of merit

for converting temperature to electricity, such as the Seebeck effect, and other effects that account for heat losses during current movement, including the Joule resistive heating effect. The Fourier heat conduction effect is also considered in the governing equations to account for the spread of heat due to conduction along the thermoelement length. The formulation of these equations requires the replacement of the terms in the heat and current density equations with thermoelectric-like terms. This has been done by making use of references [47, 49, 50], and the resulting coupled equation for temperature distribution in the thermoelectric layers is as follows:

$$\vec{\nabla} \cdot (k\vec{\nabla}T) + J^2\rho - \beta\vec{J} \cdot \vec{\nabla}T = 0 \tag{1}$$

where k is the thermal conductivity, T is the operating temperature, J is the current density, ρ is the electrical resistivity, and β is the Thomson coefficient. The terms from the left in the equation represent Fourier heat conduction, while the next term denotes Joule resistive heating, and the final term corresponds to Thomson heating. The Thomson effect is related to the exchange of heat as a result of the travel of current along the length of a thermoelectric material [51, 52]. It is a significant effect that influences the performance of thermoelectric devices. Previous studies have reported that neglecting the Thomson effect in the thermoelectric numerical model can lead to an overestimation of the thermoelectric generator performance [53, 54]. Therefore, this work considers the Thomson effect in the numerical model, defining it as [55, 56].

$$\beta = T\frac{dS}{dT} \tag{2}$$

where S is the Seebeck coefficient. However, the equation governing the electrical voltage distributions and flow of electric currents within the thermoelectric device was derived by replacing the terms in the electric charge continuity equation with thermoelectric-like terms [44, 57], resulting in the following expression [58]

$$\vec{\nabla}\cdot\left(\frac{S\vec{\nabla}T}{\rho}\right)+\vec{\nabla}\cdot\left(\frac{\vec{\nabla}\varpi}{\rho}\right)=0 \tag{3}$$

where ϖ is the electric field scalar potential. The matched load power output and energy efficiency of the device can be estimated using the following expressions [59]

$$P=\frac{(S\Delta T)^2}{4R} \tag{4}$$

$$\eta=\frac{P}{Q_{\mathrm{in}}} \tag{5}$$

where R is the internal electric resistance, and Q_{in} is the inflow heat energy. The amount of concentrated solar energy absorbed at the device top ceramic plate is calculated using the expression [60]

$$Q_{\mathrm{in}}=\mathrm{CG}A_{\mathrm{s}}\eta_{\mathrm{opt}}\alpha_{\mathrm{s}}\tau_{\mathrm{g}} \tag{6}$$

where CG is the concentrated heat flux, A_{s} is the area of the selective surface absorber, η_{opt} is the optical efficiency of the concentrator, α_{s} is the absorptivity, and τ_{g} is the transmissivity of the top glass cover. η_{opt}, α_{s}, and τ_{g} are assumed to be 0.95 [61, 62], A_s is equal to the surface area of the top ceramic plate (40 mm × 40 mm), and CG is equal to 25 $\mathrm{kWm^{-2}}$.

As solar irradiance beams on the solar concentrator top glass cover, it is not guaranteed that all of it would be converted to useful thermal energy. A fraction of the incoming solar photons is lost due to convective and radiative heat transfer processes occurring at the device hot junction. These are accounted for using [63]

$$H_{\mathrm{conv,h}}=5.82+4.07w \tag{7}$$

where $H_{\mathrm{conv,h}}$ is the convective heat transfer coefficient at the hot junction, and w is the wind speed.

$$H_{\mathrm{rad,h}}=\varepsilon\sigma\left(T_{\mathrm{h}}+T_{\mathrm{sky}}\right)\left(T_{\mathrm{h}}^2+T_{\mathrm{sky}}^2\right) \tag{8}$$

where $H_{\mathrm{rad,h}}$ is the radiative heat transfer coefficient at the hot junction, ε is the emissivity, and σ is the Stefan–Boltzmann constant, T_{h} is the hot junction temperature, and T_{sky} is the sky temperature.

where T_{sky} is obtained from [64]

$$T_{\mathrm{sky}}=0.0552T_{\mathrm{a}}^{1.5} \tag{9}$$

Bayesian neural networks

Standard neural networks, consisting of an input layer, hidden layers, and an output layer, are trained using the well-known back-propagation algorithm. The learning behavior of the network is modeled through an iterative process that continually reduces errors with each successive iteration. The learning process involves feeding training data into the input layer, processing these data through each neuron in the hidden layer, and generating corresponding outputs in the output layer. The error signal is sent back through the neurons in cases where a large deviation exists between the target values and the neural network outputs. The gradient descent algorithm is used to minimize the network's objective loss function by fine-tuning each connected mass in the negative gradient direction. The objective loss function of the network is the mean squared error, which is defined as [41]

$$E(W)=\left(\frac{1}{m}\right)\sum_{k=1}^{m}\left(T_{\mathrm{k}}-O_{\mathrm{k}}\right)^2 \tag{10}$$

where T_{k} is the target value, O_{k} is the predicted output value from the neural network, and m is the total number of data points. The summation runs over all data points.

$S(W)$, the sum of squares of the network masses is given by:

$$S(W)=\sum w_{\mathrm{i}}^2 \tag{11}$$

where w_{i} represents each mass in the network and the summation runs over all the masses in the network.

Each connected mass in the network is adjusted according to the following expression [41]

$$\Delta w_{\mathrm{ij}}=-\eta\frac{\partial E(W)}{\partial w_{\mathrm{ij}}} \tag{12}$$

where

- Δw_{ij} is the adjustment to the mass connecting neuron i in one layer to neuron j in the next layer.
- η is the learning rate, which determines the step size of the mass update during each iteration
- $E(W)$ is the objective loss function, which is typically the mean squared error (MSE) for regression tasks or cross-entropy loss for classification tasks.

- $\partial E(W)/\partial w_{ij}$ is the partial derivative of the objective function with respect to the mass w_{ij}. It represents the gradient of the error with respect to that mass.

The expression signifies that the mass update is proportional to the negative gradient of the error with respect to the mass. The learning rate, η, controls the size of the update step. A smaller learning rate results in smaller mass updates, leading to slower convergence, while a larger learning rate may result in larger mass updates, possibly overshooting the minimum and causing instability in the learning process.

The iterative process is conducted repeatedly until learning is completed when the objective function is minimized, or the total number of allowable iterations is completed. However, the standard back-propagation algorithm is a first-order gradient descent algorithm that is prone to slow convergence speeds and may become trapped in local minima during iterations.

To overcome the limitations of the first-order algorithms, Bayesian regularization is employed to modify the objective function by adding the average of the sum of squares of the network masses to the new objective function. Consequently, the modified objective function becomes: [41]

$$L(W) = E(W) + \beta S(W) \tag{13}$$

In this modified objective function, $L(W)$ represents the regularized objective function, $E(W)$ is the mean squared error as previously defined, and $S(W)$ is the sum of squares of the network masses. The term β is the regularization parameter that controls the trade-off between minimizing the mean squared error and minimizing the sum of squares of the network masses. The regularization parameter β prevents the overfitting of the model by penalizing large masses, thereby ensuring a more generalized solution.

The modified objective function can be written as:

$$\Delta w = -\eta\left(\frac{\partial L(W)}{\partial w}\right) \tag{14}$$

In this expression, Δw represents the change in masses, η is the learning rate, and $\partial L(W)/\partial w$ is the gradient of the regularized objective function with respect to the masses.

By adopting Bayesian regularization, the neural network is less prone to overfitting, and it converges faster compared to the standard back-propagation algorithm. Additionally, it requires fewer data points for training, which makes it suitable for cases with limited data availability.

Feature normalization

To balance the significance of each parameter utilized during the training process and to ease the difficulties of training, the training data are normalized. The training data are normalized between offset values of 0.1 as the minimum and 0.9 as the maximum. The data are normalized using the following equation [65]

$$X_n = \frac{\left(X - X_{min}\right)(0.9 - 0.1)}{\left(X_{max} - X_{min}\right)} + 0.1 \tag{15}$$

In this case, X_n is the normalized values of the argument, X. X_{min} and X_{max} are the minimum and maximum values of the argument, respectively. After successful training and testing of the neural network, the outputs are stored in a normalized vector. To recover the unnormalized results, the following equation is used

$$X = \frac{\left(X_n - 0.1\right)\left(X_{max} - X_{min}\right)}{(0.9 - 0.1)} + X_{min} \tag{16}$$

where X becomes the unnormalized output of X_n.

The percentage absolute relative error (PARE) is calculated using the following expression:

$$\mathrm{PARE} = \frac{\left|y_{n+1} - y_n\right|}{y_n} \times 100 \tag{17}$$

Data generation process and boundary conditions

The data used for training the neural network were obtained from three-dimensional numerical simulations conducted in ANSYS software. Seven input parameters for the numerical study were utilized, including the percentage content of skutterudite (%SKT), thermoelectric leg height (L), thermoelectric leg cross-sectional area (A), concentrated solar irradiance (CG), cold ceramic plate convective cooling coefficient ($H_{conv,cj}$), wind speed (w), and ambient temperature (T_a). The output parameters of the network involve the device power output and system efficiency. Except otherwise stated, the following boundary conditions are used to define the numerical model:

1. A heat flux of 25 $\mathrm{kWm^{-2}}$ was placed at the TEG's hot junction.
2. A convective cooling coefficient of 500 $\mathrm{Wm^{-2}\,K^{-1}}$ [66] was specified at the cold junction.
3. The ambient temperature was set to 293.15 K [67]
4. A wind speed of 1 m/s [50] was used to define the heat transfer coefficient calculated using Eq. (7) at the TEG's hot junction.
5. The surface emissivity of 0.9 [68] was used to evaluate the radiative heat transfer according to Eq. (8).
6. All external surfaces of the TEG are assumed perfectly insulated.

The device geometry is optimized for maximum power and efficiency by varying the geometry parameters in the following intervals, %SKT: 6.17–92.59%, L: 0.2–14.2 mm, and A: 0.04–2.56 mm^2. The constant values retained for the geometry parameters are %SKT = 50%, $L = 1.62$ mm, and $A = 1.96$ mm^2. Moreover, the thermal operating conditions are varied in the following interval ranges: CG: 25–161 kWm^{-2}, $H_{\mathrm{conv,cj}}$: 200–3000 Wm^{-2} K^{-1}, w: 0.5–5 ms^{-1}, T_a: 273–315 K. The computing speed used for the numerical simulation is a 64-bit operating Dell computer with a processing speed of 2.30 GHz operating on the Core i5 platform with an installed RAM of 32 GB.

Numerical model verification

A mesh convergence study was conducted to determine the optimal element size for the study, meaning the element size beyond which the output parameters of the thermoelectric device remain unchanged. To carry out this study, the mesh size of the virtual thermoelectric model was increased from coarse to fine mesh settings using the ANSYS mesh parametric convergence tool [69]. Ultimately, the numerical model was employed to reproduce experimental and theoretical results from other original research papers on a full-scale thermoelectric module, as has been done in similar numerical studies on thermoelectric generators [70, 71].

Grid independence analysis

The grid independence analysis in this study was carried out using the coarse and fine mesh settings provided by the ANSYS coupled steady-state thermal–electrical interface. A fixed heat flux of 5 kWm^{-2} and a cooling film coefficient of 3 kWm^{-2} K^{-1} were applied to define the numerical model while maintaining the other boundary conditions. The mesh quality was determined by the element size, which was parametrically varied from 0.92 mm (coarse) to 0.2 mm (fine). The results of the parametric mesh distribution are provided in Table 1. For each element size, the corresponding number of grid nodes and mesh elements is calculated, and the resulting effect of the mesh quality on the system's power output and energy efficiency is qualitatively assessed. From the results in Table 1, it can be observed that increasing mesh quality results in a higher number of grid nodes and mesh elements. Specifically, the coarse mesh generates 98,927 grid nodes and 9,244 mesh elements, while the fine mesh setting produces 2,436,205 grid nodes and 455,950 mesh elements, respectively, indicating 25 and 49 times increase in the number of nodes and elements, respectively. Generally, increasing the mesh quality implies higher numerical accuracy at the expense of computational ease. However, to ensure numerical accuracy, the independence of the system's output parameters (power and energy efficiency) on the grid nodes must be established. It is observed that the system's power and efficiency vary from 0.104 to 0.105 W and 0.804 to 0.808%, respectively. However, power and efficiency converge at the fine mesh, as the PARE is the lowest for both power ($\approx 3.1 \times 10^{-4}$) and efficiency ($\approx 1.9 \times 10^{-4}$). The PARE is computed using Eq. (17). Therefore, the fine mesh setting is deemed the optimal mesh resolution for the numerical optimization scheme.

To gain a better understanding of the grid independence study, Fig. 3 illustrates the effects of grid resolution on the three-dimensional thermal distribution of the full-scale thermoelectric module. Figure 3a and b displays the grid distribution for the coarse and fine mesh resolutions, respectively. It is evident that the fine mesh distribution contains more grids than the coarse meshing profile, particularly at the thermocouple level where thermal energy conversion occurs via thermoelectric effects. This is why the output parameters converge as the mesh element size approaches the fine mesh distribution. Furthermore, the full-scale thermoelectric module temperature distributions for the fine and coarse mesh distributions are shown in Fig. 3c and d, respectively. First,

Table 1 Grid independence results

Case	Mesh element size/mm	Grid nodes	Mesh elements	Power output/W	PARE	Energy efficiency/%	PARE
1	0.2	2,436,205	455,950	0.105219853	0.00031458	0.808772881	0.00019041
2	0.28	1,094,292	186,683	0.105219522	0.09400241	0.808771341	0.00117439
3	0.36	651,089	107,412	0.105120706	0.08911037	0.808761843	0.0052389
4	0.44	415,302	58,652	0.105214463	0.11015932	0.808719475	0.15003903
5	0.52	297,645	40,809	0.105098687	0.10173549	0.807507898	0.0243792
6	0.6	247,585	32,506	0.104991873	0.00087246	0.807311082	0.00200588
7	0.68	222,662	28,211	0.104990957	0.35242877	0.807327276	0.16808078
8	0.76	151,243	18,771	0.105362284	0.11205066	0.805972591	0.06143783
9	0.84	119,418	12,014	0.105244357	1.44495336	0.805477723	0.14794741
10	0.92	98,927	9244	0.103745286	–	0.8042878	–

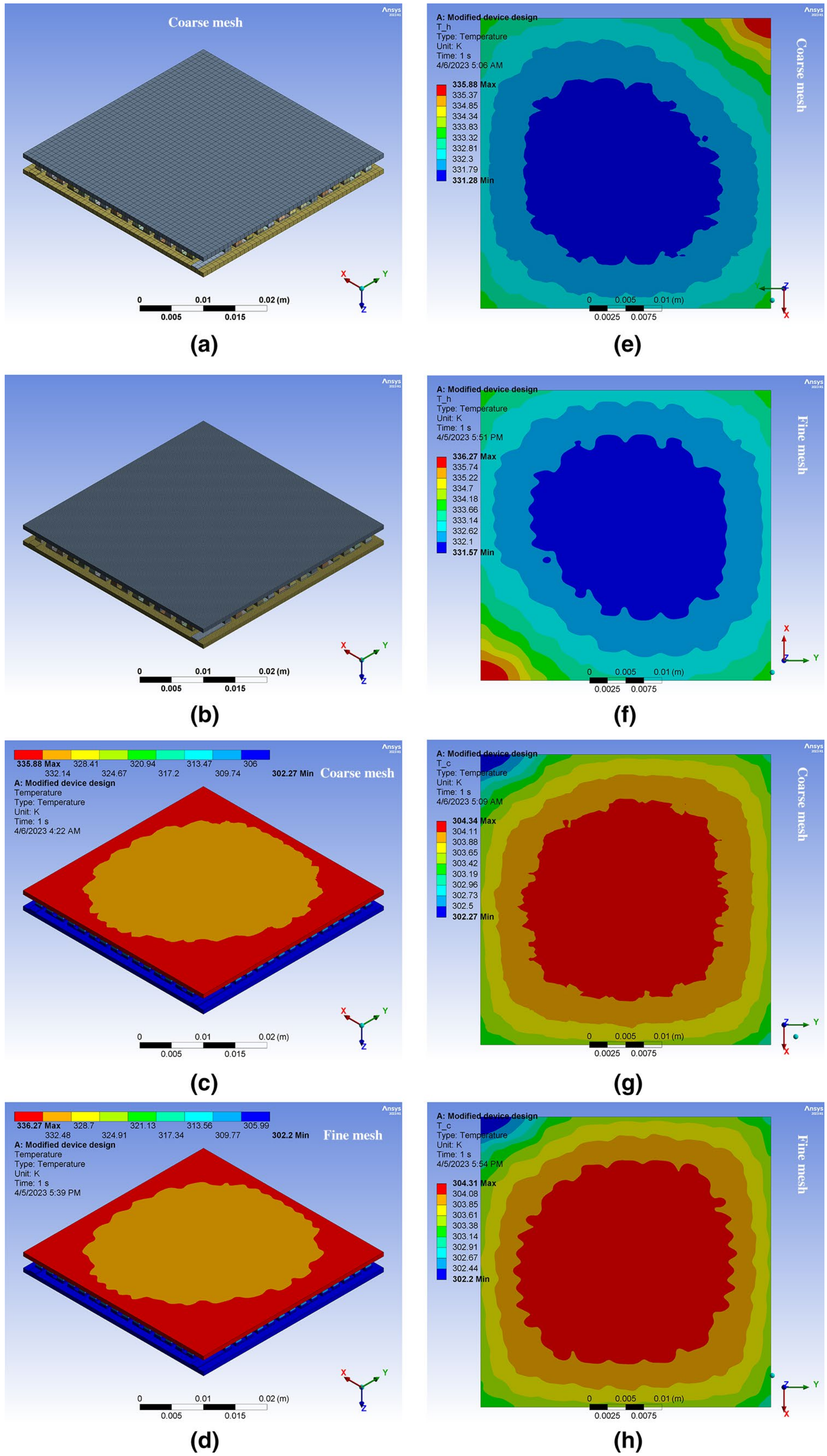

Fig. 3 Effect of mesh resolution on thermal distributions in a three-dimensional module at a concentrated thermal flux of 5 kW/m^2: **a**, **b** mesh distribution, **c**, **d** thermal distribution profile, **e**, **f** hot junction temperature profile, **g**, **h** cold junction temperature profile, **i**, **j** intermediate temperature profile of the *n*-type semiconductor, and **k**, **l** intermediate temperature profile of the *p*-type semiconductor

Fig. 3 (continued)

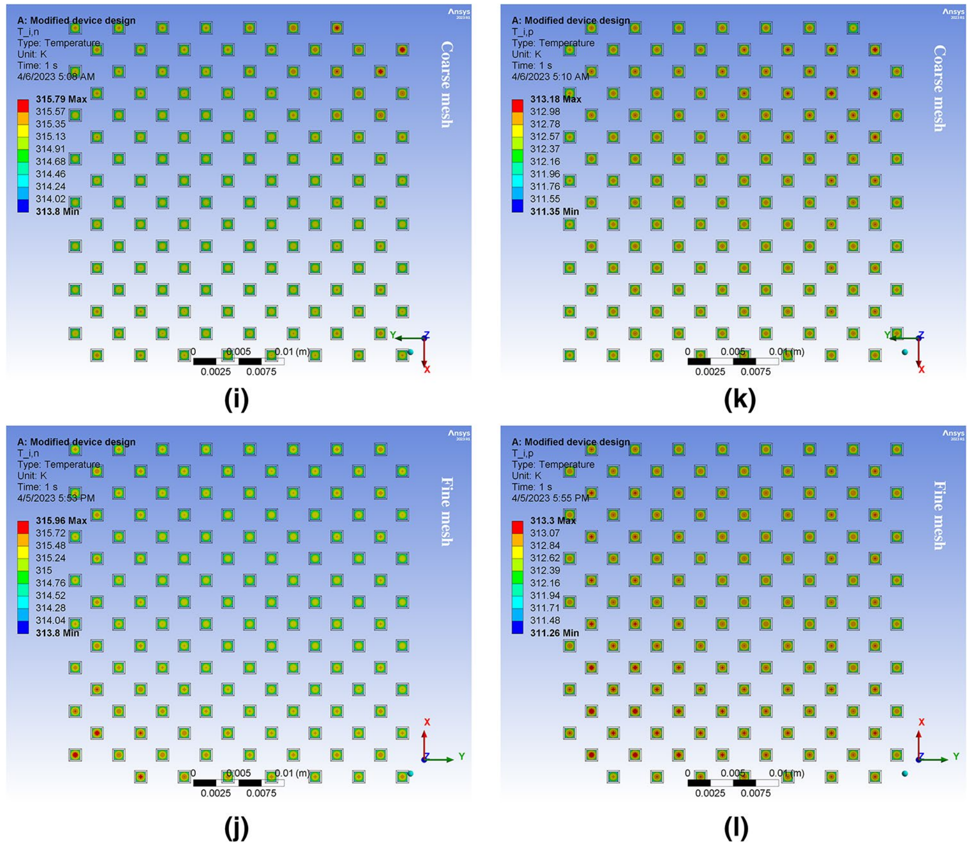

it is observed that the hot and cold junction temperatures are not uniform, as seen in Fig. 3e–h. This can be explained by considering the mutual thermocouple interaction at a relatively low heat flux of 5 kWm^{-2}. At higher heat fluxes, it is expected that the solar energy at the hot junction is absorbed more uniformly by all the thermocouples, resulting in a more uniform temperature at the hot and cold junctions. This intriguing concept is further discussed for higher heat fluxes later in this work. Overall, the hot and cold junction temperatures for the coarse and fine meshes differ due to the number of generated grids. Specifically, the hot and cold junction temperatures vary by 0.39 K and 0.07 K, respectively, between the coarse and fine distributions, while the TEG thermal gradient of the fine mesh is 0.46 K higher than that of the coarse mesh. Although 0.46 K may seem small, it could significantly impact thermoelectric module performance evaluation, given the size of the couples and their temperature-sensitive material properties. To further understand the effect of grid number on TEG thermal distribution, the ANSYS numerical scheme is tested by calculating the intermediate temperatures of the segmented thermocouple at the binding junctions of the high- and low-temperature materials. The temperature profiles are depicted in Fig. 3i, j, and k, l for the *n*-type and *p*-type semiconductors. Generally, the intermediate temperatures are not uniform but spread at different points within the module due to the mutual interaction of the couples, as discussed in the previous section. Moreover, the distributions in the *n*- and *p*-type semiconductors differ because they are distinct materials characterized by different thermal transport properties. Finally, the maximum and minimum temperatures differ for the coarse and fine mesh distributions, respectively. These differences in the hot, cold, and intermediate temperatures result in the differing power output and energy efficiencies calculated for the coarse and fine mesh distributions in Table 1.

Comparison with published experimental and numerical data

To validate the numerical model of the novel full-scale segmented variable area leg thermoelectric module, published experimental and numerical results from related studies were compared to the present numerical model. The experimental study of Fabián-Mijangos et al. [72], which validated the superior performance of variable area leg thermoelectric generators (Trap) compared to uniform leg thermoelectric generators (Rect), and the recent experimental validation section of Wang et al. [17] on the full-scale thermoelectric module were used for comparison. The numerical scheme of Li et al. [73] on variable area leg thermoelectric generators with trapezoidal cross section was also utilized for validation. The results of the comparative analysis are presented in Fig. 4, which shows a close relationship between the numerical and experimental results, with a maximum PARE of 2.4% observed in Fig. 4c and d. This indicates a good performance of the numerical model with a low PARE. The comparison with previous related experimental and numerical results demonstrates the accuracy of the present numerical model and its potential for optimizing the performance of the full-scale thermoelectric module considered in this study.

Results and discussion

This section shows the results obtained from the numerical optimization using ANSYS and the proposed neural network prediction of the device performance. The optimum design parameters for maximum power and efficiency are calculated, and the efficacy of the current optimization method in enhancing the device power and efficiency is shown.

Thermoelectric module optimization results

This section portrays the results of the design and optimization of the full-scale thermoelectric module conducted using

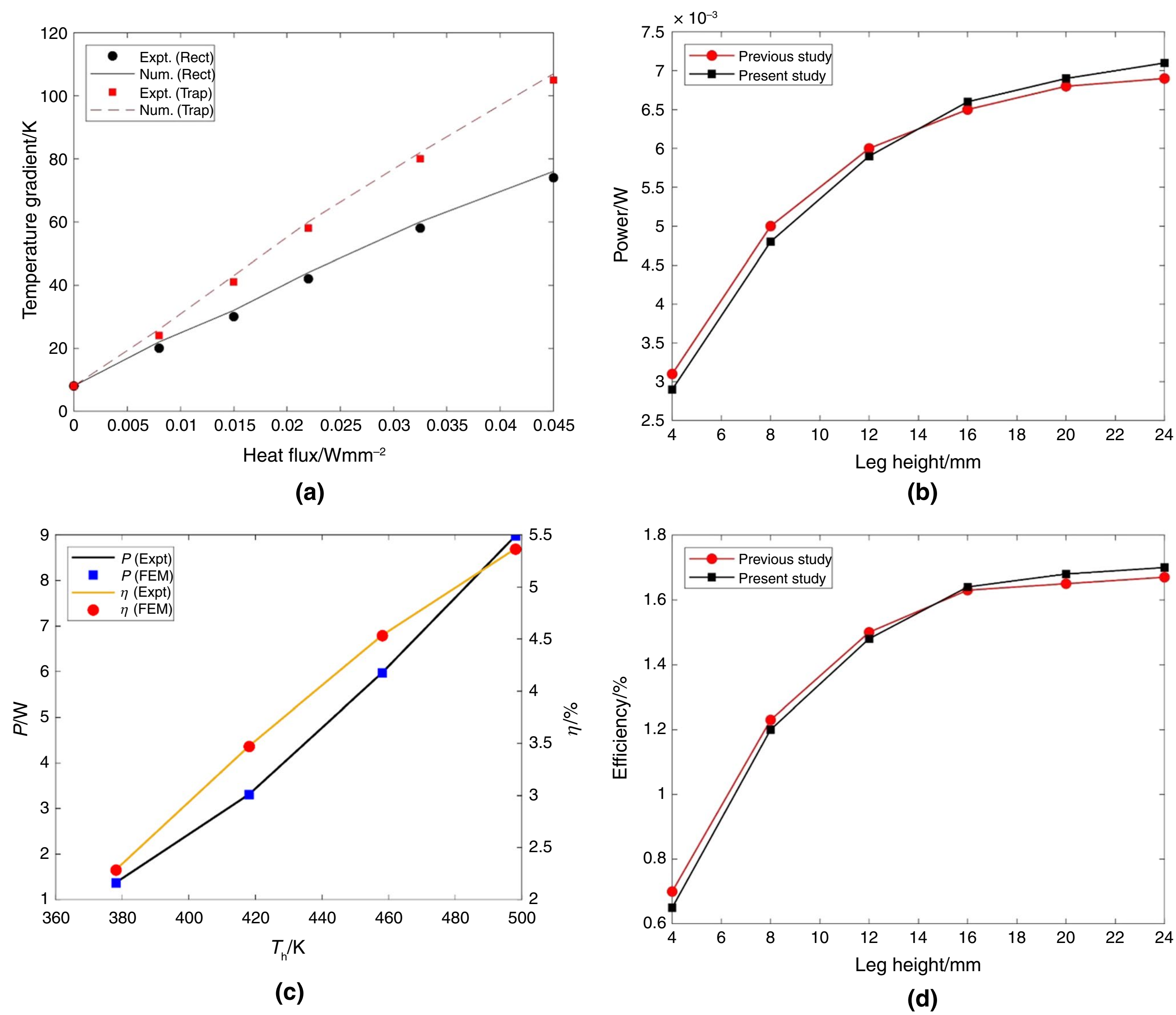

Fig. 4 Validation of the numerical model through comparison with experimental and numerical results: **a** comparison with the experimental results of Fabián-Mijangos et al. [72] on variable area leg TE couples; **b** comparison with the experimental results of Wang et al. [17] on full-scale thermoelectric module; **c**, **d** comparison with the numerical results of Li et al. [73] on variable area leg TE couples

the numerical technique setup in the ANSYS software. The results of the thermal and geometry optimization of the device are presented and discussed as well.

Solar thermal design parameters

In this study, we examined the impact of various thermal design parameters on the performance of a solar thermoelectric module. These parameters include concentrated solar irradiance, convective cooling coefficient at the cold junction, wind speed (convective film coefficient at the hot junction), and ambient temperature. The results, as shown in Fig. 5a–d, illustrate how these thermal parameters affect the module's power generation and energy efficiency.

Figure 5a demonstrates that the maximum power output and efficiency are achieved at different optimal concentrated solar irradiances: 103 kWm^{-2} and 74 kWm^{-2}, respectively. These irradiances correspond to maximum power outputs of 12.2 W and an efficiency of 4.9%. The maximum power reported here surpasses those in previous full-scale module studies [17, 29, 74], which focused on single and segmented semiconductors. This improvement is attributed to the effective combination of high- and low-temperature materials in the variable shape thermoelectric pins, while accounting for the mutual interaction between all thermocouples.

Figure 5b highlights the influence of the cold junction convective film coefficient on the power and efficiency of the thermoelectric device. Higher convective cooling film coefficients improve the overall performance of the system, as they enhance heat dissipation from the cold junction. However, increasing the film coefficient beyond 1000 $Wm^{-2} K^{-1}$ does not yield a significant performance boost.

The effects of wind speed on the system's power and efficiency are presented in Fig. 5c. Higher wind speeds impair the performance of the solar thermoelectric generator due to increased convective losses at the junction between the optical solar concentrator and the thermoelectric module's hot junction. Therefore, it is recommended to operate the solar thermoelectric module in less windy environments to minimize convection losses and maintain optimal performance.

Lastly, Fig. 5d shows the impact of ambient temperature on the thermoelectric module's performance. As the ambient temperature rises, the power and efficiency of the module decrease in a near-linear fashion. This outcome can be explained by the fact that a higher ambient temperature raises the cold junction temperature of the thermoelectric module, which results in a reduced temperature gradient and a consequent decline in the system's overall performance.

Geometry design parameters

To obtain sufficient insight into optimal geometry parameters for obtaining maximum power and efficiency from the full-scale thermoelectric module, this subsection considers the impacts of the geometry parameters of the semiconductors on the performance of the full-scale module for concentrated solar fluxes of 25, 50, 75, and 100 Suns, where 1 Sun is equivalent to 1000 Wm^{-2}. The geometry parameters considered in this optimization study are the height, cross-sectional area, and skutterudite percentage of the thermoelectric semiconductors.

Figure 5e shows the effects of the semiconductor height on the power and efficiency of the full-scale thermoelectric module for different amounts of concentrated solar energy. From the plot, it is seen that for all concentrated solar flux amounts, there exists an optimal semiconductor height that provides maximum power. On the other hand, the efficiency seems to exponentially increase as the height of the semiconductor grows. Specifically, the optimum semiconductor heights for maximum power decrease as the concentrated solar flux increases. For heat fluxes of 25, 50, 75, and 100 Suns, the optimal semiconductor heights for peak power outputs are 5.2 mm, 3.2 mm, 2.2 mm, and 1.2 mm, corresponding to maximum power outputs of 3.1 W, 7.5 W, 10.9 W, and 12.3 W, respectively, implying that at higher heat fluxes, it requires a shorter optimal semiconductor to maximize the device power generation. This is due to the higher temperatures obtained from the concentrated solar fluxes which determines the material properties of the thermoelectric material and causes the rise and fall of the device power. Nevertheless, increasing the semiconductor height elevates the module's thermal gradient which improves the energy efficiency; however, owing to the temperature dependent material properties, it is noticed that the increase in the system's efficiency decreases for longer semiconductors and that the maximum efficiency of 8.3% is obtained at a leg height of 14. 1 mm operating at 50 Suns.

Figure 5f and g displays the impacts of semiconductor cross-sectional area on the module's power and efficiency, respectively. Generally, the module's performance decreases exponentially as the semiconductor's cross-sectional area enlarges, leading to reduced thermal conductance and a smaller temperature difference. Moreover, the optimal cross-sectional area depends on the concentrated solar flux applied to the device's hot junction. As illustrated in Fig. 5g, the maximum energy efficiency of 8.3% is attained with a cross-sectional area of 0.04 mm2 at a concentrated solar flux of 50 Suns. Meanwhile, Fig. 5f demonstrates that a higher solar flux of 75 Suns is necessary to produce a peak output power of 20.1 W for the same cross-sectional area. In summary, thinner semiconductors are optimal for achieving high power and efficiency in full-scale thermoelectric modules.

The interplay between concentrated solar flux, skutterudite percentage content, and their influence on the power output and energy efficiency of the device is illustrated in Fig. 5h and i. The plot reveals that at lower solar fluxes,

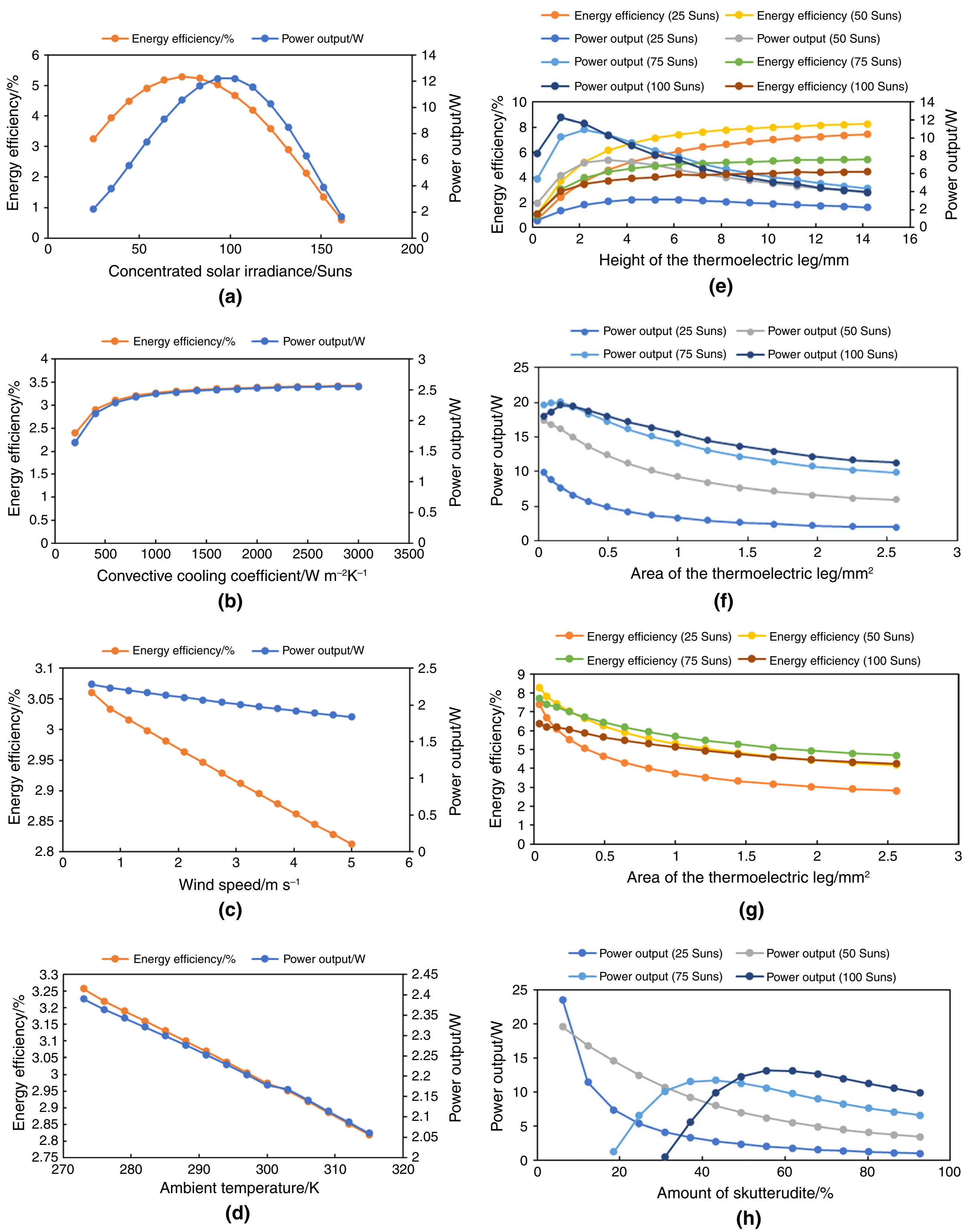

Fig. 5 Performance optimization results **a** concentrated solar flux **b** cooling film coefficient **c** wind flow speed **d** air temperature **e** semiconductor height **f**, **g** semiconductor cross-sectional area **h**, **i** amount of skutterudite

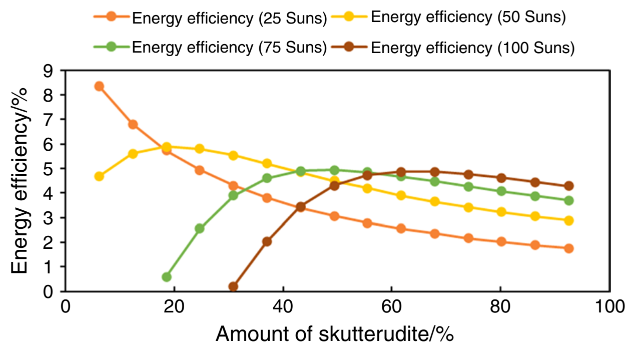

(i)

Fig. 5 (continued)

the module's power and efficiency generally decrease with increasing skutterudite content. However, as solar flux reaches higher levels, the system's performance peaks at an optimal skutterudite percentage content. This finding highlights the advantages of segmented semiconductors under high-temperature conditions due to the distribution of high- and low-temperature materials within the thermoelectric pin. In essence, for low heat fluxes, the lowest skutterudite content (predominantly bismuth telluride) yields the highest performance, while for higher heat fluxes, predominantly bismuth telluride results in the lowest performance. Maximum performance is achieved with an appropriate combination of skutterudite and bismuth telluride (segmentation). Specifically, for concentrated solar fluxes of 75 and 100 Suns, the optimal skutterudite content to generate maximum power outputs of 11.8 W and 13.2 W is 43.2% and 55.6%, respectively. Similarly, the optimal skutterudite contents for maximum energy efficiencies of 5.89%, 4.94%, and 4.87% are 18.5%, 49.4%, and 61.7%, respectively. This indicates that as the applied solar flux increases, the optimal skutterudite content required to maximize the module's performance also increases. Ultimately, the benefits of segmented thermoelectric generators in high-temperature applications are demonstrated.

Effect of device optimization

The optimization analysis results are presented in Table 2, with thermal parameters listed first followed by geometry parameters. It is observed that the geometry parameters have a more significant impact on the module's power and efficiency than the thermal parameters. Specifically, the percentage of skutterudite outperforms other parameters, generating 23.6 W of electrical power at an energy efficiency of 8.34%. Using this data, we compare the performance of the optimized module to that of the unoptimized module under the same boundary conditions to evaluate the effectiveness of the optimization approach adopted in this study. The temperature profiles and computer-aided designs of both modules are displayed in Fig. 6. The calculations reveal that the maximum power and efficiency from the optimal module are 23.6 W and 8.3%, respectively. In contrast, the unoptimized module's power output and efficiency are 2.4 W and 3.5%, respectively. By comparing the two, we deduce that the power and efficiency of the unoptimized module are increased by 875% and 165%, respectively, through optimization.

Table 2 Optimal design parameters (thermal and geometry)

S/N	Parameter	Power	Efficiency
Thermal parameters			
1	CG(Suns)	103	74
2	$h_{conv,c}$(kWm^{-2} K^{-1})	3	3
3	v(ms^{-1})	0.5	0.5
4	T_a(K)	273	273
Geometry parameters			
CG = 25 Suns	H_{te} (mm)	5.2 mm (3.2 W)	14.2 mm (7.4%)
CG = 50 Suns		3.2 mm (7.5 W)	14.2 mm (8.3%)
CG = 75 Suns		2.2 mm (10.9 W)	14.2 mm (7.6%)
CG = 100 Suns		1.2 mm (12.3 W)	14.2 mm (6.2%)
CG = 25 Suns	A_{te} (mm)	0.04 mm^2 (9.8 W)	0.04 mm^2 (7.4%)
CG = 50 Suns		0.04 mm^2 (17.3 W)	0.04 mm^2 (8.3%)
CG = 75 Suns		0.16 mm^2 (20.1 W)	0.04 mm^2 (7.7%)
CG = 100 Suns		0.16 mm^2 (19.6 W)	0.04 mm^2 (6.4%)
CG = 25 Suns	%SKT(%)	6.17% (23.6 W)	6.17% (8.34%)
CG = 50 Suns		6.17% (19.6 W)	18.5% (5.4%)
CG = 75 Suns		43.21% (11.75 W)	49.4% (4.94%)
CG = 100 Suns		55.6% (13.2 W)	61.73% (4.87%)

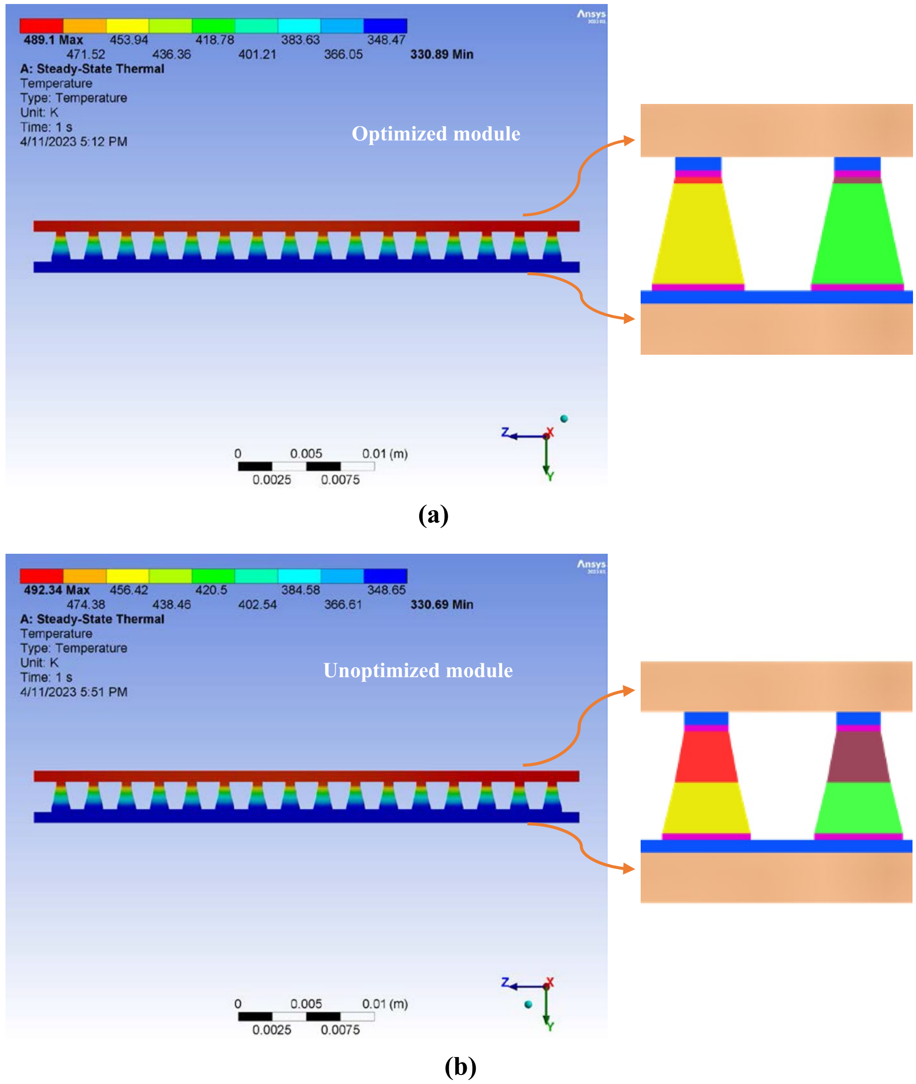

Fig. 6 Temperature profiles and computer-aided designs for full-scale thermoelectric modules **a** optimized module, **b** unoptimized module

Thermal distributions

The alteration in the temperature distribution within the segmented variable area leg thermoelectric device elements for high concentrated solar flux application, 50 and 450 kWm^{-2}, is shown in Fig. 7. The plot illustrates that increasing the incident solar flux causes the device hot and cold junction temperatures to increase due to the higher amount of thermal energy being absorbed at the device top ceramic plate for the same cooling conditions. Specifically, at low heat flux of 50 kWm^{-2}, it is noticed that the hot junction temperature is lower at the mid-section of the module while the outer section of the module maintains at a higher temperature. This phenomenon is possibly due to the interaction between the 127 thermoelectric couples in the full-scale module. Also, beyond 50 kWm^{-2}, the module's hot junction temperature becomes fully saturated with the heat flux and the temperature becomes constant both in the mid- and outer sections.

How to manufacture the proposed device

This section briefly addresses how the proposed device can be realized after the optimum geometry parameters and operating conditions have been obtained via simulation. Several methods of manufacturing the parts of thermoelectric modules exist [18, 72, 75]; however, three-dimensional (3D) printing stands out as an effective and economic means of printing thermoelectric materials and parts with complex geometries [76–78]. Different parts of the proposed segmented variable area leg thermoelectric generator can be printed by employing a metal 3D printer. For instance, direct writing 3D printers, such as the Adventure 3D-LB-Printer produced by Shenzhen Adventuretech Co., Ltd., P. R. China [79], can be used. Additionally, air-powered extrusion-based 3D printers [80], selective laser melting 3D printers [78], and multi-material 3D printers (especially for the segmented materials) can also be

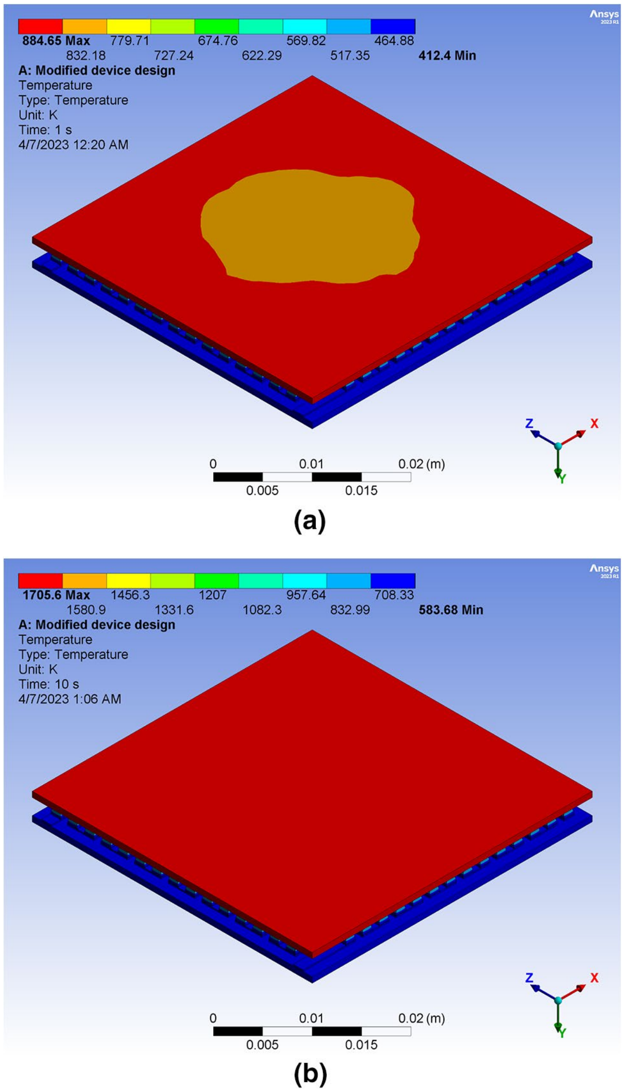

Fig. 7 Temperature distributions of the segmented variable area leg thermoelectric generator when exposed to various concentrated solar fluxes **a** 50 kWm^{-2} **b** 500 kWm^{-2}

utilized [81]. The material used for the printing is bulk semiconductors, such as bismuth-telluride for the cold segment and skutterudite for the hot segment. These materials can be drawn into filaments after a powder has been prepared using a filament extruder. Subsequently, the computer-aided designs of the device parts are sent to the 3D printer and are printed to produce the desired parts, after which they are assembled to form the device. The incident concentrated solar flux can be achieved by using a solar concentrator, such as the compound parabolic concentrator, Fresnel lens or parabolic dish. An efficient cooling system based on forced convective cooling, such as a fan or a water jet, can be used to regulate the cold side temperature to ensure optimal device performance. After the device has been tested using power generation, it can

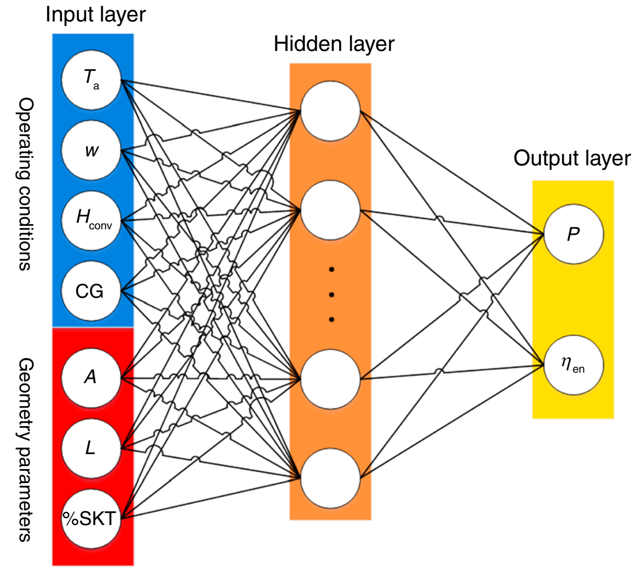

Fig. 8 Network architecture of the Bayesian regularized artificial neural network

be deployed for other applications, including waste heat recovery in solar photovoltaics, which will be the focus of a future study.

Network architectures

Ten Bayesian regularized neural network models were constructed to minimize the mean squared error and achieve high regression correlation between the numerical targets and the neural network outputs. Figure 8 depicts the architecture of the neural network, which varied in the number of neurons in the single hidden layer from 10 to 100 in increments of 10. The input parameters consisted of seven variables corresponding to the seven geometry and thermal operating conditions of the device, while the output parameters were the power and energy efficiency obtained for each case. The network diagrams show the masses and biases for each model. The Sigmoid transfer function [32, 65] was used to allow information to flow from one layer to the other. As the number of neurons increased, the complexity of the model also increased, with corresponding mean squared errors and regression coefficients recorded alongside the computational time expended during the training process for each neuron considered.

Neural network performance analysis

Figures 9 and 10 demonstrate the performance of the ten neural networks constructed to minimize the mean squared error and ensure high regression correlation between the numerical targets and neural network outputs, all regularized

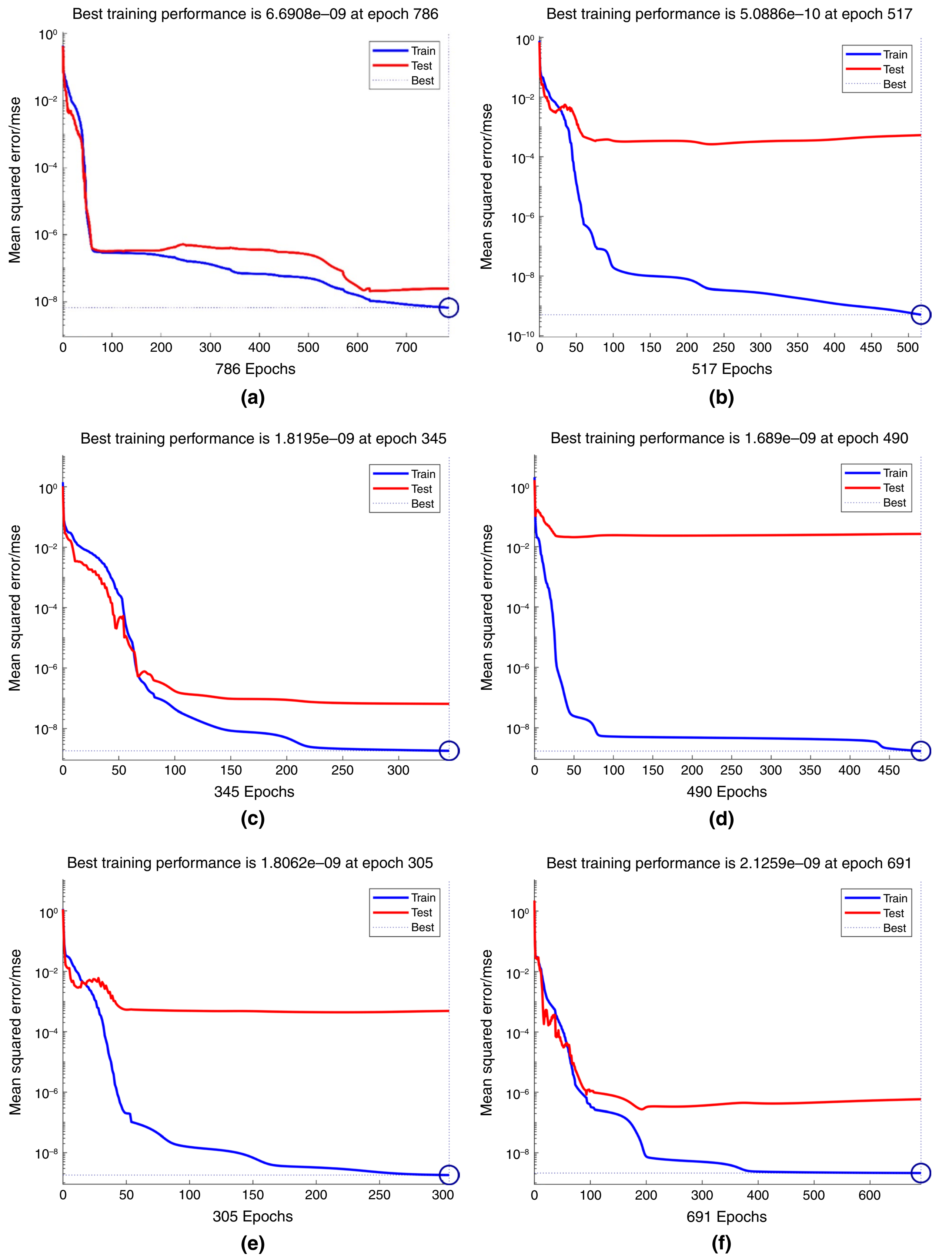

Fig. 9 Performance (mean squared error/loss function) of the Bayesian regularized artificial neural network for varying number of neurons. **a** 10 neurons **b** 20 neurons **c** 30 neurons **d** 40 neurons **e** 50 neurons **f** 60 neurons **g** 70 neurons **h** 80 neurons **i** 90 neurons **j** 100 neurons

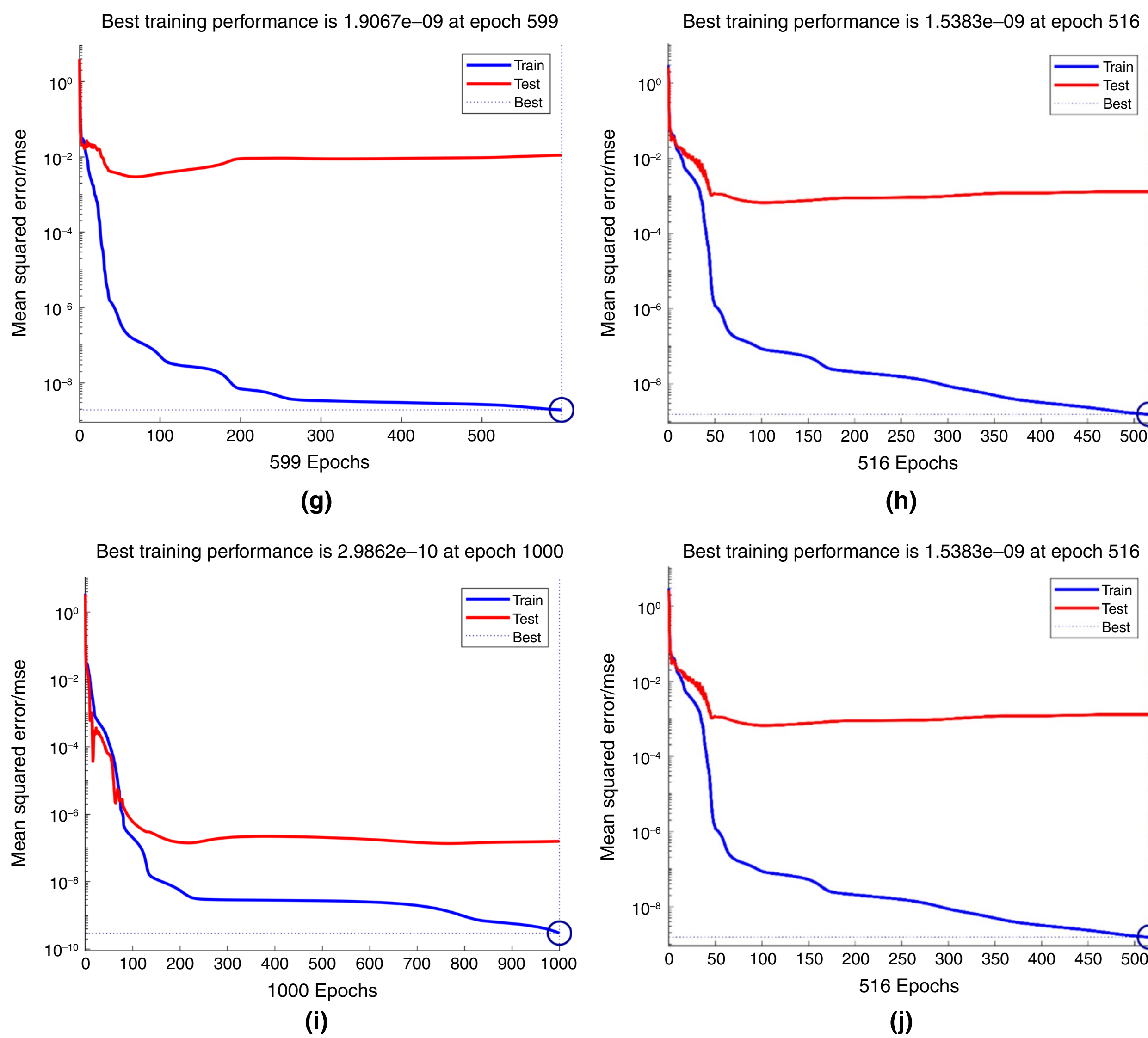

Fig. 9 (continued)

with the Bayesian algorithm. Figure 9 displays the train and test mean squared errors as the number of iterations increase, while Fig. 10 shows the regression correlations (coefficient of determination) of the ten neural networks. The number of neurons in the single hidden layer varied from 10 to 100 in steps of 10, and the input parameters were the seven geometry and thermal operating conditions of the device, while the output parameters were the power and energy efficiency obtained for each case. The masses and biases of each of the models are shown in the network diagrams, and the Sigmoid transfer function was used to allow information to flow from one layer to the other. The complexity of the models increased with the number of neurons in the hidden layer. The mean squared error and regression coefficients, along with the computational time, were recorded for each of the neurons considered.

It was observed that varying the number of neurons influenced the number of iterations completed by the neural network before approaching the optimum point, and different training and test errors were recorded when the number of neurons was sequentially varied. Increasing the number of neurons increased the network complexity, which can lead to better learning of the hidden trends in the network, particularly when the training dataset is noisy. However, if the dataset is not very complex, increasing the network complexity may not have a significant effect on the network's accuracy and might even cause overfitting. In all cases, the training error was less than the testing error, indicating that the network was not an underfitted model, and the regression plots demonstrated a good relationship between the numerical targets and neural network outputs. Almost perfect regression correlations were obtained for

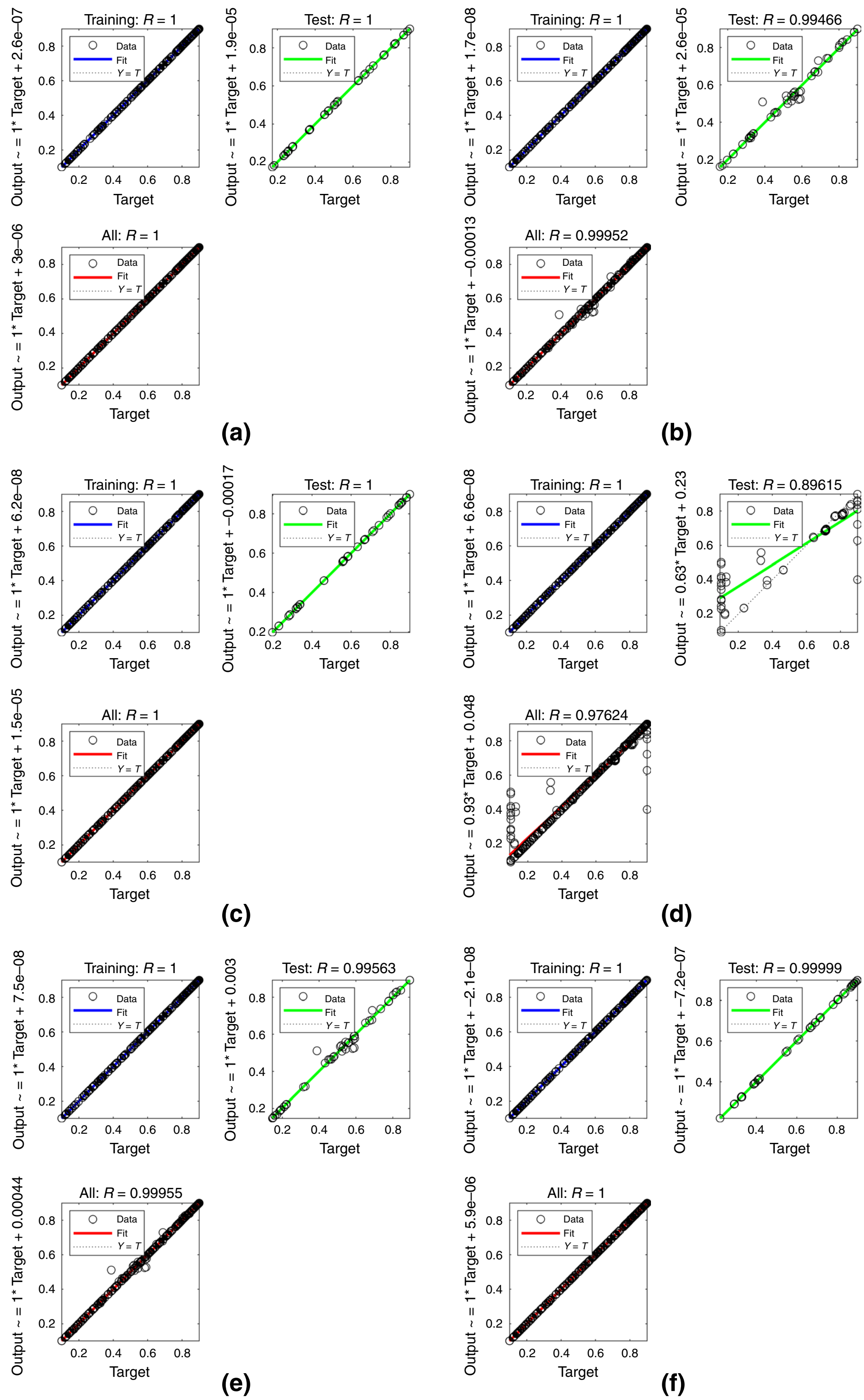

Fig. 10 Regression correlation (coefficient of determination) of the Bayesian regularized artificial neural network for varying number of neurons. **a** 10 neurons **b** 20 neurons **c** 30 neurons **d** 40 neurons **e** 50 neurons **f** 60 neurons **g** 70 neurons **h** 80 neurons **i** 90 neurons **j** 100 neurons

10, 30, 60, and 90 neurons, respectively, indicating that the best network performances were obtained with these numbers of neurons. The testing errors were slightly higher than the training errors for these cases, implying better network performances. However, for the other plots in Fig. 9, the testing errors were much higher than the training error, indicating overfitting in the model.

Fig. 10 (continued)

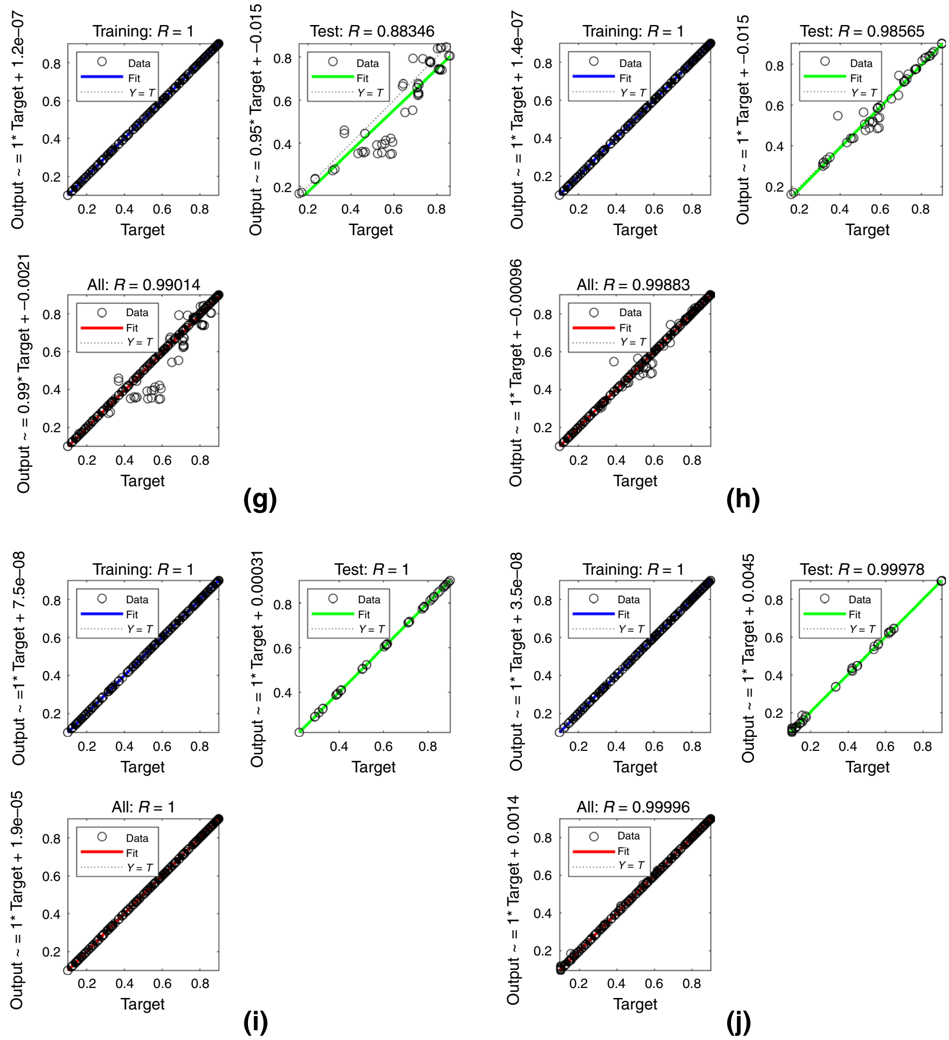

Table 3 Network training information of the Bayesian regularized artificial neural network for varying number of neurons

Number of neurons	Epochs	Elapsed time	Performance	Gradient	Mu	Effective number of parameters	Sum squared parameters
10	786	12 s	6.69×10^{-9}	9.95×10^{-8}	50	308	167
30	345	53 s	1.82×10^{-9}	1.00×10^{-7}	50	319	155
60	691	18 min, 39 s	2.13×10^{-9}	9.98×10^{-8}	50	323	159
90	1000	1 h, 43 min, 39 s	2.99×10^{-10}	1.82×10^{-7}	50	351	155

To choose the best network among the four options (10, 30, 60, and 90 neurons), we refer to the network training information provided in Table 3. Table 3 shows that increasing the number of neurons from 10 to 30, 60, and 90 raises the computational time needed to achieve the best performance. This occurs because a larger number of neurons result in a more complex system, leading to numerous intricate connections between network layers before output parameters are produced. As the primary goal of using a neural network model over a numerical model is to reduce computational time, we opt for the neural network with the shortest computational time—the network with ten neurons.

Another perspective on these results is that, since a Bayesian regularized network is employed, increasing the number of neurons may not be necessary. This is because Bayes' theorem aids in preventing overfitting or underfitting [38, 39, 82]. Moreover, the widely accepted notion that increasing the number of neurons enhances network accuracy [83–86] does not hold true in all situations.

Conclusions

This study has systematically investigated the effects of various geometry and thermal parameters on the performance of full-scale segmented variable area leg thermoelectric modules under concentrated solar flux conditions using a numerical method established in ANSYS software. The thermal parameters considered were the concentrated solar flux, convective cooling coefficient, wind speed, and air temperature. The geometry parameters examined were the semiconductor height, cross-sectional area, and percentage skutterudite content. Through a comprehensive optimization analysis, the optimal parameters for maximizing power output and energy efficiency were identified. A Bayesian regularized neural network was proposed to fit the generated data, enabling the timely obtainment of design parameters. The key findings of this research include:

1. The geometry parameters, particularly the percentage of skutterudite, height, and cross-sectional area of the thermoelectric semiconductors, have a more significant impact on the module's performance compared to the thermal parameters.
2. Optimal semiconductor height and cross-sectional area were found to depend on the level of concentrated solar flux. Higher solar fluxes necessitate shorter optimal semiconductors and thinner cross-sectional areas to maximize power generation and efficiency.
3. The optimal skutterudite content increases as the applied solar flux rises, demonstrating the benefits of segmented thermoelectric generators in high-temperature applications, such as optically concentrated solar systems.
4. The optimization approach employed in this study resulted in a substantial improvement in both power output and efficiency for the full-scale thermoelectric module. The optimized module's power output and efficiency increased by 875% and 165%, respectively, compared to the unoptimized module at 25 Suns.
5. The proposed Bayesian regularized neural network with just 10 hidden neurons and few data points accurately learned the numerical data, achieving a low mean squared error of 6.7×10^{-9} and a high coefficient of determination of 1 on testing and training datasets.

In conclusion, this research provides valuable insights into the optimization of full-scale thermoelectric modules under concentrated solar flux conditions. The findings can serve as a guide for the design and development of high-performance thermoelectric modules for various applications, particularly in harnessing solar energy for sustainable power generation. Further research could explore the integration of advanced materials and novel module designs to enhance performance and adaptability to a broader range of operating conditions.

Subsequent research will seek to fabricate the proposed thermoelectric modules and test them under experimental conditions to ascertain and further validate their performance for possible prototyping.

Acknowledgements The authors appreciate the following funding agencies: the Deanship of Scientific Research at Najran University for funding this work under the research groups funding program grant code (NU/RG/SERC/12/16), the Deanship of Scientific Research at King Faisal University for funding this work under the research collaboration funding program grant number Grant A048, the Office of Research and Sponsored Programs (ORSP) at Abu Dhabi University for funding this paper through a research fund.

Funding 'Open Access funding provided by the MIT Libraries'.

Data availability The data used in this work can be made available upon reasonable request from the corresponding author.

References

1. Zhao Y, Li W, Diao H, Wang Y, Ge M. Experimental research of solar thermoelectric generator based on flat heat pipe. Energy Rep. 2022;8:245–50. https://doi.org/10.1016/j.egyr.2022.05.193.
2. Lv JR, Ma JL, Dai L, Yin T, He ZZ. A high-performance wearable thermoelectric generator with comprehensive optimization of thermal resistance and voltage boosting conversion. Appl Energy. 2022;312:118696. https://doi.org/10.1016/j.apenergy.2022.118696.
3. Wang Y-P, Chen W, Huang Y-Y, Liu X, Su C-Q. Performance study on a thermoelectric generator with exhaust-module-coolant direct contact. Energy Rep. 2022;8:729–38. https://doi.org/10.1016/j.egyr.2022.05.228.
4. Mamur H, Dilmaç ÖF, Begum J, Bhuiyan MRA. Thermoelectric generators act as renewable energy sources. Clean Mater. 2021;2:100030. https://doi.org/10.1016/j.clema.2021.100030.
5. Zhang F, Cheng L, Wu M, Xu X, Wang P, Liu Z. Performance analysis of two-stage thermoelectric generator model based on Latin hypercube sampling. Energy Convers Manag. 2020;221:113159. https://doi.org/10.1016/j.enconman.2020.113159.
6. Shoeibi S, Kargarsharifabad H, Sadi M, Arabkoohsar A, Mirjalily SAA. A review on using thermoelectric cooling, heating, and electricity generators in solar energy applications. Sustain Energy

Technol Assess. 2022;52:102105. https://doi.org/10.1016/j.seta.2022.102105.

7. Chen Y, Xie B, Long J, Kuang Y, Chen X, Hou M, Gao J, Zhou S, Fan B, He Y, Zhang Y-T, Wong C-P, Wang Z, Zhao N. Interfacial laser-induced graphene enabling high-performance liquid−solid triboelectric nanogenerator. Adv Mater. 2021;33:2104290. https://doi.org/10.1002/adma.202104290.
8. Liu Z, Li J, Liu X. Novel functionalized BN nanosheets/epoxy composites with advanced thermal conductivity and mechanical properties. ACS Appl Mater Interfaces. 2020;12:6503–15. https://doi.org/10.1021/acsami.9b21467.
9. Shittu S, Li G, Zhao X, Ma X. Review of thermoelectric geometry and structure optimization for performance enhancement. Appl Energy. 2020;268:1–31. https://doi.org/10.1016/j.apenergy.2020.115075.
10. Lal Sharma S, Debbarma A. Effect of P-Leg material and resistance ratio on a segmented thermoelectric generator. Mater Today Proc. 2022. https://doi.org/10.1016/j.matpr.2022.04.825.
11. Cao J, Tan XY, Jia N, Zheng J, Chien SW, Ng HK, Tan CKI, Liu H, Zhu Q, Wang S, Zhang G, Chen K, Li Z, Zhang L, Xu J, Hu L, Yan Q, Wu J, Suwardi A. Designing good compatibility factor in segmented $Bi_{0.5}Sb_{1.5}Te_3$–GeTe thermoelectrics for high power conversion efficiency. Nano Energy. 2022;96:107147. https://doi.org/10.1016/j.nanoen.2022.107147.
12. Zhao J, Xu W, Kuang Z, Long R, Liu Z, Liu W. Segmental material design in thermoelectric devices to boost heat-to-electricity performance. Energy Convers Manag. 2021;247:114754. https://doi.org/10.1016/j.enconman.2021.114754.
13. Demeke W, Kim Y, Jung J, Chung J, Ryu B, Ryu S. Neural network-assisted optimization of segmented thermoelectric power generators using active learning based on a genetic optimization algorithm. Energy Rep. 2022;8:6633–44. https://doi.org/10.1016/j.egyr.2022.04.065.
14. Al-Merbati AS, Yilbas BSS, Sahin AZZ. Thermodynamics and thermal stress analysis of thermoelectric power generator : influence of pin geometry on device performance. Appl Therm Eng. 2013;50:683–92. https://doi.org/10.1016/j.applthermaleng.2012.07.021.
15. Weng Z, Liu F, Zhu W, Li Y, Xie C, Deng J, Huang L. Performance improvement of variable-angle annular thermoelectric generators considering different boundary conditions. Appl Energy. 2022;306:118005. https://doi.org/10.1016/j.apenergy.2021.118005.
16. Ge Y, He K, Xiao L, Yuan W, Huang S-M. Geometric optimization for the thermoelectric generator with variable cross-section legs by coupling finite element method and optimization algorithm. Renew Energy. 2022;183:294–303. https://doi.org/10.1016/j.renene.2021.11.016.
17. Wang X, Qi J, Deng W, Li G, Gao X, He L, Zhang S. An optimized design approach concerning thermoelectric generators with frustum-shaped legs based on three-dimensional multiphysics model. Energy. 2021;233:120810. https://doi.org/10.1016/j.energy.2021.120810.
18. Mohammad Siddique AR, Mahmud S, Van Heyst B. Performance comparison between rectangular and trapezoidal-shaped thermoelectric legs manufactured by a dispenser printing technique. Energy. 2020;196:117089. https://doi.org/10.1016/j.energy.2020.117089.
19. Wang P, Wang B, Wang K, Gao R, Xi L. An analytical model for performance prediction and optimization of thermoelectric generators with varied leg cross-sections. Int J Heat Mass Transf. 2021. https://doi.org/10.1016/j.ijheatmasstransfer.2021.121292.
20. Liu HB, Meng JH, Wang XD, Chen WH. A new design of solar thermoelectric generator with combination of segmented materials and asymmetrical legs. Energy Convers Manag. 2018;175:11–20. https://doi.org/10.1016/j.enconman.2018.08.095.
21. Shittu S, Li G, Zhao X, Ma X, Golizadeh Y, Ayodele E. Optimized high performance thermoelectric generator with combined segmented and asymmetrical legs under pulsed heat input power. J Power Sources. 2019;428:53–66. https://doi.org/10.1016/j.jpowsour.2019.04.099.
22. Luo Y, Li L, Chen Y, Kim CN. Influence of geometric parameter and contact resistances on the thermal-electric behavior of a segmented TEG. Energy. 2022;254:124487. https://doi.org/10.1016/j.energy.2022.124487.
23. Abdolrasol MGM, Suhail Hussain SM, Ustun TS, Sarker MR, Hannan MA, Mohamed R, Ali JA, Mekhilef S, Milad A. Artificial neural networks based optimization techniques: a review. Electronics (Switzerland). 2021. https://doi.org/10.3390/electronics10212689.
24. Sarker IH. Deep learning: a comprehensive overview on techniques, taxonomy, applications and research directions, SN computer. Science. 2021;2:420. https://doi.org/10.1007/s42979-021-00815-1.
25. Emmert-Streib F, Yang Z, Feng H, Tripathi S, Dehmer M. An introductory review of deep learning for prediction models with big data. Front Artif Intell. 2020;3:1–23. https://doi.org/10.3389/frai.2020.00004.
26. Pang Z, Niu F, O'Neill Z. Solar radiation prediction using recurrent neural network and artificial neural network: a case study with comparisons. Renew Energy. 2020;156:279–89. https://doi.org/10.1016/j.renene.2020.04.042.
27. Mazzeo D, Herdem MS, Matera N, Bonini M, Wen JZ, Nathwani J, Oliveti G. Artificial intelligence application for the performance prediction of a clean energy community. Energy. 2021;232:120999. https://doi.org/10.1016/j.energy.2021.120999.
28. Garud KS, Jayaraj S, Lee MY. A review on modeling of solar photovoltaic systems using artificial neural networks, fuzzy logic, genetic algorithm and hybrid models. Int J Energy Res. 2021;45:6–35. https://doi.org/10.1002/er.5608.
29. Kishore R, Mahajan R, Priya S. Combinatory finite element and artificial neural network model for predicting performance of thermoelectric generator. Energies. 2018;11:2216. https://doi.org/10.3390/en11092216.
30. Zhu Y, Newbrook DW, Dai P, de Groot CHK, Huang R. Artificial neural network enabled accurate geometrical design and optimisation of thermoelectric generator. Appl Energy. 2022;305:117800. https://doi.org/10.1016/j.apenergy.2021.117800.
31. Ang ZYA, Woo WL, Mesbahi E. Artificial neural network based prediction of energy generation from thermoelectric generator with environmental parameters. J Clean Energy Technol. 2017;5:458–63. https://doi.org/10.18178/JOCET.2017.5.6.416.
32. Garud KS, Seo J-H, Cho C-P, Lee M-Y. Artificial neural network and adaptive neuro-fuzzy interface system modelling to predict thermal performances of thermoelectric generator for waste heat recovery. Symmetry. 2020;12:259. https://doi.org/10.3390/sym12020259.
33. Angeline AA, Asirvatham LG, Hemanth DJ, Jayakumar J, Wongwises S. Performance prediction of hybrid thermoelectric generator with high accuracy using artificial neural networks. Sustain Energy Technol Assess. 2019;33:53–60. https://doi.org/10.1016/j.seta.2019.02.008.
34. Okulu D, Selimefendigil F, Öztop HF. Review on nanofluids and machine learning applications for thermoelectric energy conversion in renewable energy systems. Eng Anal Bound Elem. 2022;144:221–61. https://doi.org/10.1016/j.enganabound.2022.08.004.
35. Kim TY. Prediction of system-level energy harvesting characteristics of a thermoelectric generator operating in a diesel engine

using artificial neural networks. Energies. 2021;14:2426. https://doi.org/10.3390/en14092426.
36. Wang P, Wang K, Xi L, Gao R, Wang B. Fast and accurate performance prediction and optimization of thermoelectric generators with deep neural networks. Adv Mater Technol. 2021;6:2100011. https://doi.org/10.1002/admt.202100011.
37. Burden F, Winkler D, Bayesian regularization of neural networks. In: Methods in molecular biology; 2008. pp. 23–42. https://doi.org/10.1007/978-1-60327-101-1_3.
38. Okut H. Bayesian Regularized Neural Networks for Small n Big p Data. In: Artificial neural networks—models and applications, InTech. 2016. pp. 1–22. https://doi.org/10.5772/63256.
39. Sariev E, Germano G. Bayesian regularized artificial neural networks for the estimation of the probability of default. Quant Finance. 2020;20:311–28. https://doi.org/10.1080/14697688.2019.1633014.
40. Caballero J, Fernández M. Linear and nonlinear modeling of antifungal activity of some heterocyclic ring derivatives using multiple linear regression and Bayesian-regularized neural networks. J Mol Model. 2006;12:168–81. https://doi.org/10.1007/s00894-005-0014-x.
41. Wu D, Huang H, Qiu S, Liu Y, Wu Y, Ren Y, Mou J. Application of Bayesian regularization back propagation neural network in sensorless measurement of pump operational state. Energy Rep. 2022;8:3041–50. https://doi.org/10.1016/j.egyr.2022.02.072.
42. Sun Z, Chen Y, Li X, Qin X, Wang H. A Bayesian regularized artificial neural network for adaptive optics forecasting. Opt Commun. 2017;382:519–27. https://doi.org/10.1016/j.optcom.2016.08.035.
43. Yang B, Li D, Zeng C, Chen Y, Guo Z, Wang J, Shu H, Yu T, Zhu J. Parameter extraction of PEMFC via Bayesian regularization neural network based meta-heuristic algorithms. Energy. 2021;228:120592. https://doi.org/10.1016/j.energy.2021.120592.
44. Shittu S, Li G, Xuan Q, Zhao X, Ma X, Cui Y. Electrical and mechanical analysis of a segmented solar thermoelectric generator under non-uniform heat flux. Energy. 2020;199:117433. https://doi.org/10.1016/j.energy.2020.117433.
45. Erturun U, Erermis K, Mossi K. Effect of various leg geometries on thermo-mechanical and power generation performance of thermoelectric devices. Appl Therm Eng. 2014;73:126–39. https://doi.org/10.1016/j.applthermaleng.2014.07.027.
46. Erturun U, Erermis K, Mossi K. Influence of leg sizing and spacing on power generation and thermal stresses of thermoelectric devices. Appl Energy. 2015;159:19–27. https://doi.org/10.1016/j.apenergy.2015.08.112.
47. Maduabuchi CC, Mgbemene CA. Numerical study of a phase change material integrated solar thermoelectric generator. J Electron Mater. 2020;49:5917–36. https://doi.org/10.1007/s11664-020-08331-3.
48. Mgbemene CA, Njoku HO, Agbo COA. Investigation of parametric performance of the hybrid 3D CPC/TEM system due to thermoelectric irreversibilities. Front Energy Res. 2018;6:1–11. https://doi.org/10.3389/fenrg.2018.00101.
49. Maduabuchi C. Improving the performance of a solar thermoelectric generator using nano-enhanced variable area pins. Appl Therm Eng. 2022;206:118086. https://doi.org/10.1016/j.applthermaleng.2022.118086.
50. Maduabuchi C. Thermo-mechanical optimization of thermoelectric generators using deep learning artificial intelligence algorithms fed with verified finite element simulation data. Appl Energy. 2022;315:118943. https://doi.org/10.1016/j.apenergy.2022.118943.
51. Maduabuchi C, Lamba R, Ozoegwu C, Njoku HO, Eke M, Gurevich YG, Ejiogu EC. Thomson effect and nonlinear performance of thermoelectric generator. Heat Mass Transf. 2022;58:967–80. https://doi.org/10.1007/s00231-021-03153-3.
52. Badillo-ruiz CA, Olivares-robles MA, Ruiz-ortega PE. Performance of segmented thermoelectric cooler micro-elements with different geometric shapes and temperature-dependent properties. Entropy. 2018;20:1–17. https://doi.org/10.3390/e20020118.
53. Singh S, Isreal O, Lamba R. Thermodynamic evaluation of irreversibility and optimum performance of a concentrated PV-TEG cogenerated hybrid system. Sol Energy. 2018;170:896–905. https://doi.org/10.1016/j.solener.2018.06.034.
54. Fraisse G, Ramousse J, Sgorlon D, Goupil C. Comparison of different modeling approaches for thermoelectric elements. Energy Convers Manag. 2013;65:351–6. https://doi.org/10.1016/j.enconman.2012.08.022.
55. Maduabuchi CC, Ejenakevwe KA, Mgbemene CA. Performance optimization and thermodynamic analysis of irreversibility in a contemporary solar thermoelectric generator. Renew Energy. 2021;168:1189–206. https://doi.org/10.1016/j.renene.2020.12.130.
56. Kaushik SC, Manikandan S, Hans R. Energy and exergy analysis of an annular thermoelectric heat pump. J Electron Mater. 2016;45:3400–9. https://doi.org/10.1007/s11664-016-4465-x.
57. Ebiringa MA, Adimonyemma JP, Maduabuchi C. Performance evaluation of a nanomaterial-based thermoelectric generator with tapered legs. Glob J Energy Technol Res Updates. 2020;7:48–54. https://doi.org/10.15377/2409-5818.2020.07.5.
58. Maduabuchi C, Njoku H, Eke M, Mgbemene C, Lamba R, Ibrahim JS. Overall performance optimisation of tapered leg geometry based solar thermoelectric generators under isoflux conditions. J Power Sources. 2021;500:229989. https://doi.org/10.1016/j.jpowsour.2021.229989.
59. Alghamdi H, Maduabuchi C, Mbachu DS, Albaker A, Alatawi I, Alsenani TR, Alsafran AS, AlAqil M. Machine learning model for transient exergy performance of a phase change material integrated-concentrated solar thermoelectric generator. Appl Therm Eng. 2023. https://doi.org/10.1016/j.applthermaleng.2023.120540.
60. Kraemer D, Jie Q, McEnaney K, Cao F, Liu W, Weinstein LA, Loomis J, Ren Z, Chen G. Concentrating solar thermoelectric generators with a peak efficiency of 7.4%. Nat Energy. 2016;1:16153. https://doi.org/10.1038/nenergy.2016.153.
61. Lamba R, Kaushik SC. Solar driven concentrated photovoltaic-thermoelectric hybrid system: numerical analysis and optimization. Energy Convers Manag. 2018;170:34–49. https://doi.org/10.1016/j.enconman.2018.05.048.
62. Candadai AA, Kumar VP, Barshilia HC. Solar Energy Materials & Solar Cells Performance evaluation of a natural convective-cooled concentration solar thermoelectric generator coupled with a spectrally selective high temperature absorber coating. Solar Energy Mater Solar Cells. 2015. https://doi.org/10.1016/j.solmat.2015.10.040.
63. Notton G, Cristofari C, Mattei M, Poggi P. Modelling of a double-glass photovoltaic module using finite differences. Appl Therm Eng. 2005;25:2854–77. https://doi.org/10.1016/j.applthermaleng.2005.02.008.
64. Eke MN, Maduabuchi CC, Lamba R, Njoku HO, Ma X, Gurevich YG, Tyagi SK, Ekechukwu OV, Ejiogu EC, Eneh CT. Exergy analysis and optimisation of a two-stage solar thermoelectric generator with tapered legs. Int J Exergy. 2022;38:110. https://doi.org/10.1504/IJEX.2022.122309.
65. Gangi Setti S, Rao RN. Artificial neural network approach for prediction of stress–strain curve of near β titanium alloy. Rare Met. 2014;33:249–57. https://doi.org/10.1007/s12598-013-0182-2.
66. Shittu S, Li G, Tang X, Zhao X, Ma X, Badiei A. Analysis of thermoelectric geometry in a concentrated photovoltaic-thermoelectric

under varying weather conditions. Energy. 2020;202:1–13. https://doi.org/10.1016/j.energy.2020.117742.
67. Maduabuchi CC, Eke MN, Mgbemene CA. Solar power generation using a two-stage X-leg thermoelectric generator with high-temperature materials. Int J Energy Res. 2021;45:13163–81. https://doi.org/10.1002/er.6644.
68. Li G, Diallo TMO, Akhlaghi YG, Shittu S, Zhao X, Ma X, Wang Y. Simulation and experiment on thermal performance of a micro-channel heat pipe under different evaporator temperatures and tilt angles. Energy. 2019;179:549–57. https://doi.org/10.1016/j.energy.2019.05.040.
69. Patil H, Jeyakarthikeyan PV. Mesh convergence study and estimation of discretization error of hub in clutch disc with integration of ANSYS. In: IOP conference series: materials science and engineering; 2018. vol. 402, p. 012065. https://doi.org/10.1088/1757-899X/402/1/012065.
70. Shittu S, Li G, Zhao X, Ma X, Akhlaghi YG, Ayodele E. High performance and thermal stress analysis of a segmented annular thermoelectric generator. Energy Convers Manag. 2019;184:180–93. https://doi.org/10.1016/j.enconman.2019.01.064.
71. Lee M-Y, Seo J, Lee H, Garud KS. Power generation efficiency and thermal stress of thermoelectric module with leg geometry, material, segmentation and two-stage arrangement. Symmetry. 2020;12:786. https://doi.org/10.3390/sym12050786.
72. Fabián-Mijangos A, Min G, Alvarez-Quintana J. Enhanced performance thermoelectric module having asymmetrical legs. Energy Convers Manag. 2017;148:1372–81. https://doi.org/10.1016/j.enconman.2017.06.087.
73. Li G, Shittu S, Ma X, Zhao X. Comparative analysis of thermoelectric elements optimum geometry between photovoltaic-thermoelectric and solar thermoelectric. Energy. 2019;171:599–610. https://doi.org/10.1016/j.energy.2019.01.057.
74. Kishore RA, Sanghadasa M, Priya S. Optimization of segmented thermoelectric generator using Taguchi and ANOVA techniques. Sci Rep. 2017;7:16746. https://doi.org/10.1038/s41598-017-16372-8.
75. Siddique ARM, Venkateshwar K, Mahmud S, Van Heyst B. Performance analysis of bismuth-antimony-telluride-selenium alloy-based trapezoidal-shaped thermoelectric pallet for a cooling application. Energy Convers Manag. 2020;222:113245. https://doi.org/10.1016/j.enconman.2020.113245.
76. Thimont Y, LeBlanc S. The impact of thermoelectric leg geometries on thermal resistance and power output. J Appl Phys. 2019;126:095101. https://doi.org/10.1063/1.5115044.
77. Burton MR, Mehraban S, Beynon D, McGettrick J, Watson T, Lavery NP, Carnie MJ. 3D printed SnSe thermoelectric generators with high figure of merit. Adv Energy Mater. 2019. https://doi.org/10.1002/aenm.201900201.
78. Qiu J, Yan Y, Luo T, Tang K, Yao L, Zhang J, Zhang M, Su X, Tan G, Xie H, Kanatzidis MG, Uher C, Tang X. 3D Printing of highly textured bulk thermoelectric materials: mechanically robust BiSbTe alloys with superior performance. Energy Environ Sci. 2019;12:3106–17. https://doi.org/10.1039/C9EE02044F.
79. Su N, Zhu P, Pan Y, Li F, Li B. 3D-printing of shape-controllable thermoelectric devices with enhanced output performance. Energy. 2020;195:116892. https://doi.org/10.1016/j.energy.2019.116892.
80. Kim F, Kwon B, Eom Y, Lee JE, Park S, Jo S, Park SH, Kim B-S, Im HJ, Lee MH, Min TS, Kim KT, Chae HG, King WP, Son JS. 3D printing of shape-conformable thermoelectric materials using all-inorganic Bi_2Te_3-based inks. Nat Energy. 2018;3:301–9. https://doi.org/10.1038/s41560-017-0071-2.
81. Yang SE, Kim F, Ejaz F, Lee GS, Ju H, Choo S, Lee J, Kim G, Jung S, Ahn S, Chae HG, Kim KT, Kwon B, Son JS. Composition-segmented BiSbTe thermoelectric generator fabricated by multimaterial 3D printing. Nano Energy. 2021;81:105638. https://doi.org/10.1016/j.nanoen.2020.105638.
82. Zhang X, Sun L, Qi L. Bayesian regularization algorithm based recurrent neural network method and NSGA-II for the optimal design of the reflector. Machines. 2022. https://doi.org/10.3390/machines10010063.
83. Kim H-C, Kang M-J. A comparison of methods to reduce overfitting in neural networks. Int J Adv Smart Converg. 2020;9:173–8.
84. Li H, Li J, Guan X, Liang B, Lai Y, Luo X. Research on overfitting of deep learning. In: Proceedings—2019 15th International Conference on Computational Intelligence and Security, CIS 2019; 2019. pp. 78–81. https://doi.org/10.1109/CIS.2019.00025.
85. Ying X. An Overview of Overfitting and its Solutions. In: Journal of physics conference series; 2019. vol. 1168. https://doi.org/10.1088/1742-6596/1168/2/022022.
86. Srivastava N, Hinton G, Krizhevsky A, Sutskever I, Salakhutdinov R. Dropout: a simple way to prevent neural networks from overfitting. J Mach Learn Res. 2014;15:1929–58.